Ultraviolet cascade in the thermalization of the classical ϕ^4 theory in 3 + 1 dimensions

C. Destri[1,*] and H. J. de Vega[2,†]

[1]*Dipartimento di Fisica G. Occhialini, Università Milano-Bicocca Piazza della Scienza 3, 20126 Milano, Italy and INFN, sezione di Milano, via Celoria 16, Milano, Italy*

[2]*LPTHE, Université Pierre et Marie Curie, Paris VI et Denis Diderot, Paris VII, Laboratoire Associé au CNRS UMR 7589, Tour 24, 5ème. étage, 4, Place Jussieu, 75252 Paris, Cedex 05, France and Observatoire de Paris, LERMA, Laboratoire Associé au CNRS UMR 8112, 61, Avenue de l'Observatoire, 75014 Paris, France*

(Received 5 October 2005; published 19 January 2006)

We investigate the dynamics of thermalization and the approach to equilibrium in the classical ϕ^4 theory in 3 + 1 spacetime dimensions. The nonequilibrium dynamics is studied by numerically solving the equations of motion in a light-cone-like discretization of the model for a broad range of initial conditions and energy densities. A smooth cascade of energy towards the ultraviolet is found to be the basic mechanism of thermalization. After an initial transient stage, at a time scale of several hundred inverse masses, the squared magnitude of the field spatial gradient becomes larger than the nonlinear term and there emerges a stage of universal cascade, independent of the details of the initial conditions. As the cascade progresses, the modes with higher wave numbers, but well behind the forefront of the cascade, exhibit weaker and weaker nonlinearities well described by the Hartree approximation, while the infrared modes retain strong self-interactions. As a consequence, two time scales for equilibration appear as characteristic of two time-dependent wave number regions. For $k^2 \gtrsim \overline{\phi^2}(t)$, we observe an effective equilibration to a time-dependent powerlike spectrum with a time scale in the hundreds of inverse masses; cutoff effects are absent and the Hartree approximation holds for $k^2 \gg \overline{\phi^2}(t)$. On the other hand, infrared modes with $k^2 \lesssim \overline{\phi^2}(t)$ equilibrate only by time scales in the millions of inverse masses when the cutoff effects become dominant and complete thermalization is setting in. Accordingly, we observe in the field correlator a relatively large and long-lived deviation from the Hartree behavior of a nonperturbative character. There corresponds an effective mass governing the long distance behavior of the correlator which turns out to be significantly smaller than the Hartree mass which is exhibited by the modes with $k^2 \gtrsim \overline{\phi^2}(t)$. Virialization and the equation of state start to set in much earlier than thermalization. The applicability of these results in quantum field theory for large occupation numbers and small coupling is analyzed.

DOI: 10.1103/PhysRevD.73.025014 PACS numbers: 11.10.−z, 05.45.Pq, 12.38.Mh, 98.80.Cq

I. INTRODUCTION

The understanding of the dynamics of thermalization and relaxation in a field theory is a subject of critical importance both in early cosmology as well as in ultrarelativistic heavy ion collisions.

Pioneering work in this topic was initiated by Fermi, Pasta, and Ulam [1] for a chain of coupled oscillators. Since then, this problem has been studied within a variety of models [2] with the goal of answering fundamental questions on ergodicity, equipartition, and in general the approach to equilibrium in nonlinear theories with a large but finite number of degrees of freedom.

By understanding the dynamics of thermalization we mean to uncover in detail the mechanisms that lead to thermal states starting from arbitrary initial conditions as well as to determine the time scales of these phenomena. In cosmology the inflationary paradigm *assumes* that after the inflationary stage a period of particle production and relaxation leads to a state of local thermal equilibrium thus merging inflation with the standard hot big bang cosmology [3,4].

Inflationary scenarios lead to particle production either via parametric amplification of fluctuations of the inflaton (in the case of an oscillating inflaton) or by spinodal instabilities during phase transitions [5–8]. In both cases the nonequilibrium dynamics is nonperturbative and results in a large population of soft quanta whose dynamics is nearly classical. The nonequilibrium dynamics of particle production and eventual thermalization are nonperturbative and the resulting fluctuations contribute to the evolution of the scale factor, namely, the backreaction from the fluctuations becomes important in the evolution of the cosmological spacetime [5–8]. Both parametric amplification and spinodal decomposition lead to nonperturbative particle production of a band of wave vectors, typically for soft momenta [5–8]. This nonperturbative large population allows a classical treatment of the nonequilibrium evolution. Thermalization may be described in this classical framework or one can implement the quantum 2-particles irreducible (2PI) framework in cosmological spacetimes.

In this article we study the nonequilibrium dynamics going towards thermalization in the classical ϕ^4 theory in 3 + 1 dimensions. As mentioned above the initial stages of nonequilibrium dynamics either in cosmology or in ultrarelativistic heavy ion collisions is mainly *classical*. Classical field theory must be understood with an ultravio-

*Electronic address: Claudio.Destri@mib.infn.it
†Electronic address: devega@lpthe.jussieu.fr

let cutoff, or equivalently an underlying lattice spacing, to avoid the Rayleigh-Jeans catastrophe.

The advantage of studying the classical field theory is that the equation of motion can be solved exactly. Contrary to quantum theory, there is no need for making approximations. Classical field theory is expected to be a good approximation to the quantum theory for large occupation numbers and small coupling as we argue in this paper.

We provide a detailed understanding of the *main dynamical mechanisms* that lead to thermalization and to study the approach to thermalization by several different observables. We address several questions on the equilibrium and nonequilibrium aspects: (i) what are the criteria for thermalization in an interacting theory, (ii) what is the mechanism that leads to thermalization, (iii) what is the dynamics for different observables, how do they reach thermal equilibrium, and which are the relevant time scales?

We focus our study on these issues within the context of classical field theory, which is an interesting and timely problem all by itself. It is also *likely* to describe the initial stages of evolution strongly out of equilibrium in quantum theory for the relevant cases of very large occupation numbers and small coupling.

The main results of this work are the following:

(i) We implement a discretization of the φ^4 model in any number of spacetime dimensions which is very accurate and stable, maintains the relativistic symmetry between space and time, and conserves energy exactly (that is to machine accuracy on a computer). The same discretization scheme, restricted to space alone, can be used to study the model at canonical equilibrium through Monte Carlo simulations.

(ii) We provide the main physical properties of the classical φ^4 model in thermal equilibrium using low temperature perturbative expansions as well as Monte Carlo simulations. These simulations show that the leading order perturbative results have a large domain of validity, further extended by the Hartree approximation, except for infrared modes, which retain a strong nonperturbative character.

(iii) We extensively investigate the dynamics of the φ^4 model for a wide range of (infrared supported) initial conditions and energy densities. After a first stage with relatively important fluctuations whose precise structure depends on the details of the initial conditions, the model evolves towards a universal stage where energy transfer from low to high wave numbers becomes steady and very effective, resulting in a steady smooth ultraviolet cascade. Namely, the power spectrum of the field ϕ and its canonical momentum π acquire support in a monotonic and slow way over larger and larger values of the wave vectors. This ultraviolet cascade leads to an efficient transfer of energy from π^2, ϕ^2, and the interaction terms ϕ^4 to the spatial gradient $(\nabla\phi)^2$ which grows monotonically. Therefore, there is a crossover during this stage from a strong to a weak interacting theory since the nonlinear term ϕ^4 becomes much smaller than the spatial gradients. The average wave number $\overline{k}(t)$ of the modes grows monotonically with time approximately as $t^{1/3}$. The universal stage is well established by a time $t_0 \simeq 500$ (in inverse mass units) which does not depend on the lattice spacing and depends weakly on the energy density E/V as long as E/V is not very small. The study of the ϕ and $\pi = \dot{\phi}$ correlators allows us to obtain the power spectrum of ϕ and π which exhibits universal scaling properties during the smooth cascade. We find that virialization sets rather fast at times $t \gtrsim t_0$. Parallel to virialization, the equation of state approaches the radiation equation. Namely, the ratio of the pressure divided by the energy density approaches $\frac{1}{3}$ for energy densities not too small as the nonlinearities weaken. The ultraviolet cascade continues till the lattice cutoff is reached and therefore the universal properties with respect to the discretization method are lost. These cutoff effects become important long before full thermalization of the power spectra sets in, but late enough for small enough lattice spacing for the window of the universal cascade to be clearly visible.

(iv) The infrared modes with $k^2 \lesssim \overline{\phi^2}(t)$ exhibit a much slower dynamics than the rest of the modes. The modes with $\overline{k}(t) \gg k^2 \gg \phi^2$ are well described by the Hartree approximation and equilibrate effectively by times $\sim t_0 \simeq 500$ (in inverse mass units) while the infrared modes reach an equilibrium state only by times $t \sim 10^6$, when $\overline{k}(t)$ is very close to the UV cutoff. In this equilibrium state a rather large deviation from Hartree behavior remains for low wave numbers. In configuration space the correlation length turns out to be $1/M_{\rm eff}(t)$ where the effective mass of the infrared modes $M_{\rm eff}(t)$ is substantially smaller than the Hartree mass. Therefore, there are two scales for equilibration: the shorter one t_0 characterizes the UV cascade evolution, the local magnitudes as the time average $\overline{\phi^2}(t)$ and the modes with $k^2 \gtrsim \overline{\phi^2}(t)$, while the longer scale governs the evolution of the infrared modes $k^2 \lesssim \overline{\phi^2}(t)$.

(v) The thermalization process in $3 + 1$ dimensions is quite different from that in $1 + 1$, studied with the same light-cone-like discretization approach in Ref. [9], although a universal smooth ultraviolet cascade is present in both cases. In the $1 + 1$ case the cascade of the π power spectrum is characterized by a single universal shape function with the time evolution reducing to a scale transformation

on such a function. On the contrary, in $D = 3 + 1$, one can still define a shape function for the cascade but it turns out to be time dependent; in particular, there exists a window at intermediate values of the scaled wave number $k/\overline{k}(t)$ with a powerlike behavior, but the power depends markedly on time even when cutoff effects are fully negligible. Most remarkably, the shape function is almost flat near the origin in $1 + 1$ dimensions, allowing one to consistently define an effective thermalization which, starting from the deep infrared where power is concentrated at zero time, progresses to higher wave numbers with a well-defined effective temperature monotonically decreasing in time. In $D = 3 + 1$ instead, the deep infrared is the last to thermalize and the mode equilibration in the bulk of the cascade, where powerlike spectra are observed, cannot be characterized only by a time-dependent effective temperature.

Nonetheless, the notion of a time-dependent effective temperature keeps its sense for specific (simple) observables also in $3 + 1$ dimensions. For instance, from the late time behavior of π^2, ϕ^2, ϕ^4, and $(\nabla\phi)^2$ one can read off an effective temperature which monotonically decreases with time approximately as $\sim t^{-1/3}$. This effective temperature reaches the proper nonzero limit in the lattice for very late times showing that true thermalization has been achieved. In the continuum this effective temperature would always vanish for infinite time.

(vi) Although all our present work (and in Ref. [9]) deals with classical field theory, some of the main features such as the ultraviolet cascade and the slow thermalization dynamics of the infrared modes should be relevant in quantum field theory (QFT) for large occupation numbers and small coupling.

The main message to early cosmology and ultrarelativistic heavy ion collision physics from the present work is that thermalization proceeds very slowly in classical field theory (at least for unbroken symmetry in scalar models). However, a state of effective equilibration is soon reached and is characterized by a steady, smooth, and relatively simple cascade of energy flowing towards the ultraviolet. The natural interpretation is that the ''fast'' degrees of freedom have indeed reached some sort of statistical equilibrium defined by a few macroscopic parameters (such as the temperature, but not the temperature alone) which are slowly varying in time. On the continuum, without any cutoff effect for arbitrary long time, this effective temperature should become the only relevant slow-varying quantity for late enough time; it would eventually vanish for infinite time in classical theory, while in quantum theory it should reach a finite nonzero value necessarily involving $\hbar$.

Thermalization has been reached in quantum field theories by numerical studies in $3 + 1$ and $2 + 1$ dimensions in Refs. [10–12], respectively. In these works the 2PI expansion to lowest order and the analogous Kadanoff-Baym approximation are used, respectively. The couplings considered are quite strong and do not allow a direct connection with the classical dynamics investigated in the present paper. The numerical studies previously reported on the dynamics of classical and quantum field theories [13–17] have not yet focused on studying the mechanism of energy transfer from long to short wavelengths as a function of time. In Ref. [13] the emergence of spatiotemporal structures is reported for a symmetry breaking ϕ^4 model. Reference [14] studies the evolution of the classical $1 + 1$-dimensional ϕ^4 model. For further work in this domain see Refs. [18–20].

It would indeed be interesting to study if the universal cascade found in the classical theory [9] remains at least during some early and intermediate stages in the quantum theory.

Reference [21] investigates the classical in the $3 + 1$-dimensional massless ϕ^4 model. The ultraviolet cascade is present in their numerical results. In addition, an analytic scenario for the scaling behavior is proposed following the transport treatment of weak wave turbulence [22]. However, this heuristic treatment does not fully capture the thermalization dynamics found in $1 + 1$ dimensions in [9] as well as in $3 + 1$ dimensions in the present paper.

This paper is organized as follows: in Sec. II we present the classical ϕ^4 model in the continuum and in the lattice and our way to perform suitable coarse grainings. Section III discusses the classical ϕ^4 model in thermodynamic equilibrium and its properties both from perturbative as well as Monte Carlo calculations. Section IV is the core of the article where the dynamics of thermalization is presented. We study the time evolution of local observables as well as the correlators whose Fourier transforms yield the power spectra of the field ϕ and its conjugate momentum π. The early virialization and the late thermalization of the infrared modes are discussed. Section V contains discussions and conclusions while four appendixes deal with more specific topics.

II. THE MODEL IN THE CONTINUUM AND ON THE LATTICE

Besides defining the classical ϕ^4 model, we present in this section its lattice version simultaneously discretizing space and time in such a way that an exactly conserved lattice energy can be defined. The average procedure over the basic physical observables is presented too.

A. Basic definitions and notations

The Lagrangian density of the $(3 + 1)$-dimensional φ^4 field theory reads

$$\mathcal{L}_{m,\lambda}(\varphi) = \frac{1}{2}\partial_\mu\varphi\partial^\mu\varphi - \frac{m^2}{2}\varphi^2 - \frac{\lambda}{4}\varphi^4,$$

where $\partial_\mu \equiv \partial/\partial x^\mu$, $\mu = 0, 1, 2, 3$. This leads to the clas-

sical equation of motion

$$\partial_\mu \partial^\mu \varphi + m^2 \varphi + \lambda \varphi^3 = 0. \tag{2.1}$$

In 3 + 1 spacetime dimensions and standard units $\hbar = c = 1$, the coupling λ is dimensionless while φ has the dimensions of a mass.

At the classical level one can always rescale the coordinates and the field using some reference mass M and absorb the coupling λ in the field. Thus setting

$$\varphi(x) = \frac{M}{\sqrt{\lambda}} \phi(Mx) \tag{2.2}$$

and renaming $(Mt, M\boldsymbol{x})$ as $(t, \boldsymbol{x})$ yields for the dimensionless field ϕ the equation

$$\ddot{\phi} - \nabla^2 \phi + \gamma \phi + \phi^3 = 0,$$

where $\dot{\phi} \equiv \partial\phi/\partial t$, $\nabla_j \phi \equiv \partial\phi/\partial x_j$, and $\gamma \equiv m^2/M^2$. If $m^2 > 0$, then we can choose $M = m$ and study the parameter-free equation

$$\ddot{\phi} - \nabla^2 \phi + \phi + \phi^3 = 0. \tag{2.3}$$

This is our choice, having assumed a massive φ. At any rate, the important point here is that, unlike in QFT, the notion of a coupling constant at the classical level is not absolute as it can be scaled out.

In terms of ϕ and its canonical conjugate momentum $\pi = \dot{\phi}$, the Hamiltonian is the standard sum of a kinetic plus a potential term

$$H[\pi, \phi] = \mathcal{T}[\pi] + \mathcal{V}[\phi], \qquad \mathcal{T}[\pi] = \frac{1}{2} \int d^3x \pi^2,$$
$$\mathcal{V}[\phi] = \frac{1}{2} \int d^3x \left[(\nabla\phi)^2 + \phi^2 + \frac{1}{2}\phi^4 \right]. \tag{2.4}$$

This Hamiltonian is dimensionless; the energy of the original field φ in the standard dimension-full coordinates is given by $(m/\lambda)H[\pi, \phi]$.

We consider the model restricted to a finite volume, which we take to be the cube of side L (in units of m^{-1}) and volume $V = L^3$; we assume periodic boundary conditions (PBC), namely, $\phi(\boldsymbol{x} + L\boldsymbol{n}, t) = \phi(\boldsymbol{x}, t)$ for any $\boldsymbol{n} = (n_1, n_2, n_3) \in \mathbb{Z}^3$.

In terms of standard Fourier mode amplitudes,

$$\tilde{\pi}_{\boldsymbol{k}} = \int_V \frac{d^3x}{V^{1/2}} e^{-i\boldsymbol{k}\cdot\boldsymbol{x}} \pi(\boldsymbol{x}) = \tilde{\pi}^*_{-\boldsymbol{k}},$$
$$\tilde{\phi}_{\boldsymbol{k}} = \int_V \frac{d^3x}{V^{1/2}} e^{-i\boldsymbol{k}\cdot\boldsymbol{x}} \phi(\boldsymbol{x}) = \tilde{\phi}^*_{-\boldsymbol{k}}, \quad \boldsymbol{k} = \frac{2\pi}{L}\boldsymbol{n}, \quad \boldsymbol{n} \in \mathbb{Z}^3, \tag{2.5}$$

the Hamiltonian reads

$$H[\phi, \pi] = \frac{1}{2} \sum_{\boldsymbol{k}} \left[|\tilde{\pi}_{\boldsymbol{k}}|^2 + (1 + \boldsymbol{k}^2) |\tilde{\phi}_{\boldsymbol{k}}|^2 + \frac{1}{2V} \sum_{\boldsymbol{q}\boldsymbol{q}'} \tilde{\phi}_{\boldsymbol{q}} \tilde{\phi}_{\boldsymbol{q}'} \tilde{\phi}_{\boldsymbol{k}} \tilde{\phi}_{-\boldsymbol{q}-\boldsymbol{q}'-\boldsymbol{k}} \right].$$

The wave numbers $\boldsymbol{k}$ are dimensionless; their dimension-full counterparts are given by $m\boldsymbol{k}$.

B. Regularization on a finite space lattice

For any numerical treatment it is necessary to discretize space and time over some lattice. This obviously introduce an ultraviolet cutoff Λ over the wave numbers of the order of the inverse of the lattice spacing. To discretize the space we consider the cubic lattice $(2a\mathbb{Z})^3$, a being half the lattice spacing. Taking into account the finite size L, we obtain regularized fields

$$\phi_{\boldsymbol{n}} = \phi(\boldsymbol{x}), \qquad \pi_{\boldsymbol{n}} = \pi(\boldsymbol{x}), \qquad \boldsymbol{x} = 2a\boldsymbol{n}, \qquad \boldsymbol{n} \in C_N,$$

where C_N is the cubic subset of $\mathbb{Z}^3$ formed by integer triples (n_1, n_2, n_3) satisfying $-N/2 + 1 \le n_j \le N/2$, $j = 1, 2, 3$. Here $N = L/(2a)$ is assumed even and N^3 is clearly the total number of degrees of freedom of the regularized fields.

Owing to PBC, to the cube $2aC_N$ in x space there corresponds the dual cube $(2\pi/L)C_N$ (the so-called first Brillouin zone) of wave numbers $\boldsymbol{k}$ fulfilling

$$\boldsymbol{k} = \frac{2\pi}{L}\boldsymbol{n}, \qquad -N/2 + 1 \le n_j \le N/2, \qquad j = 1, 2, 3.$$

The largest value of each component of $\boldsymbol{k}$, $\Lambda = (2\pi/L) \times (N/2) = \pi/(2a)$, is the UV cutoff.

The lattice form of the Hamiltonian is not unique, being restricted solely by the requirement to formally reduce to the continuum expression Eq. (2.4) in the $a \to 0$ limit. For all ultralocal terms, with fields at coincident points, one could assume the simplest discretization as sums of one-site terms. Thus the kinetic energy $\mathcal{T}$ would read on the lattice

$$\mathcal{T}[\pi] = \frac{1}{2} \sum_{\boldsymbol{n} \in C_N} (2a)^3 \pi^2_{\boldsymbol{n}}, \tag{2.6}$$

and similarly for the space integrals of ϕ^2 and ϕ^4. The integral of the gradient term $(\nabla\phi)^2$ is converted, through integration by parts, to the integral of $-\phi\nabla^2\phi$, with ∇^2 the Laplacian. Then, in order to define the theory on the lattice, ∇^2 is replaced by a discretized Laplacian. The simplest choice is the nearest-neighbor form that leads to the well-known replacement of the spectrum k^2 on the continuum

$$k^2 \to \hat{k}^2, \qquad \hat{k} \equiv \frac{\sin ka}{a}.$$

However, our choice of discretization is different, as we show in the next section.

C. Discretized dynamics on a spacetime lattice

In order to solve numerically the evolution equations for the ϕ^4 theory, it is necessary to discretize time besides space. In most approaches, space and time discretization are performed separately. As discussed in the previous

section, space discretization turns the field theory into a classical dynamical problem with finitely many "coordinates" and "momenta." Their evolution is governed by ordinary differential equations which eventually require some discretization of time to be solved numerically. Here we proceed in a different way, treating space and time in a symmetric way. This generalizes the scheme introduced in 1 + 1 dimensions [9,23].

In our approach space and time are simultaneously discretized, with the same lattice spacing $2a$, in a staggered fashion over the lattice $\mathbb{Z}^{D+1} \cup (\mathbb{Z} + 1/2)^{D+1}$ (for the sake of generality, we consider here a space of generic dimensionality D). In other words the discretized spacetime points are

$$(\boldsymbol{x}, t) = a(\boldsymbol{n}, s),$$

where the integer components of $(\boldsymbol{n}, s)$ are either all even or all odd. This allows, as we shall see, to protect to a large extent the relativistic invariance of the continuum field equation (2.3) and to provide an exactly conserved energy on the lattice.

Let us first of all define the averages over local cubes of field powers

$$\Phi^{(p)}(\boldsymbol{x}, t) = \frac{1}{2^D}\sum_{\boldsymbol{\sigma}}[\phi(\boldsymbol{x} + a\boldsymbol{\sigma}, t)]^p, \qquad p = 0, 1, 2, \ldots, \tag{2.7}$$

where $\boldsymbol{\sigma} = (\sigma_1, \sigma_2, \ldots, \sigma_D)$, $\sigma_i = \pm$, $i = 1, 2, \ldots, D$. We then construct two lattice versions of relevant continuum observables through the correspondences

$$\begin{aligned}
\dot{\phi}(\boldsymbol{x}, t) \equiv \pi(\boldsymbol{x}, t) &\leftarrow \pi_\pm(\boldsymbol{x}, t) \\
&\equiv \pm a^{-1}[\phi(\boldsymbol{x}, t \pm a) - \Phi^{(1)}(\boldsymbol{x}, t)], \\
\phi^2(\boldsymbol{x}, t) \leftarrow \phi^2_\pm(\boldsymbol{x}, t) &\equiv \tfrac{1}{2}[\phi^2(\boldsymbol{x}, t \pm a) + \Phi^{(2)}(\boldsymbol{x}, t)], \\
\phi^4(\boldsymbol{x}, t) \leftarrow \phi^4_\pm(\boldsymbol{x}, t) &\equiv \phi^2(\boldsymbol{x}, t \pm a)\Phi^{(2)}(\boldsymbol{x}, t), \\
(\nabla\phi)^2(\boldsymbol{x}, t) \leftarrow (D\phi)^2(\boldsymbol{x}, t) &\equiv a^{-2}\{\Phi^{(2)}(\boldsymbol{x}, t) - [\Phi^{(1)}(\boldsymbol{x}, t)]^2\}.
\end{aligned} \tag{2.8}$$

By construction, the lattice quantities on the right-hand side tend to the continuum expressions in the limit $a \to 0$. Therefore the lattice energy densities

$$\mathcal{E}_\pm(\boldsymbol{x}, t) = \tfrac{1}{2}(2a)^D[\pi^2_\pm + (D\phi)^2 + \phi^2_\pm + \tfrac{1}{2}\phi^4_\pm]$$

both tend to the continuum energy density as $a \to 0$,

$$\mathcal{E}_\pm \simeq \mathcal{E} \equiv \tfrac{1}{2}d^D x[\dot{\phi}^2 + (\nabla\phi)^2 + \phi^2 + \tfrac{1}{2}\phi^4]$$

upon the natural identification $(2a)^D \simeq d^D x$. Notice that $\mathcal{E}_\pm$ can be explicitly written as

$$\begin{aligned}
\mathcal{E}_\pm(\boldsymbol{x}, t) = \frac{1}{2}a^{D-2}\sum_{\boldsymbol{\sigma}}&[\phi(\boldsymbol{x}, t \pm a) - \phi(\boldsymbol{x} + a\boldsymbol{\sigma}, t)]^2 \\
&+ \frac{1}{4}(2a)^D[1 + \phi^2(\boldsymbol{x}, t \pm a)] \\
&\times \left[1 + \frac{1}{2^D}\sum_{\boldsymbol{\sigma}}\phi^2(\boldsymbol{x} + a\boldsymbol{\sigma}, t)\right] - \frac{1}{4}(2a)^D,
\end{aligned} \tag{2.9}$$

which shows that only diagonal, spacetime symmetric finite differences are present.

To higher orders in a, $\mathcal{E}$ and $\mathcal{E}_\pm$ do differ; in fact

$$\begin{aligned}
\mathcal{E}_+(\boldsymbol{x}, t) - \mathcal{E}_-(\boldsymbol{x}, t) = 4(2a)^{D-2}&[\phi(\boldsymbol{x}, t + a) \\
&- \phi(\boldsymbol{x}, t - a)]Q(\boldsymbol{x}, t),
\end{aligned}$$

where

$$\begin{aligned}
Q(\boldsymbol{x}, t) = \tfrac{1}{2}&[\phi(\boldsymbol{x}, t + a) + \phi(\boldsymbol{x}, t - a)] \\
&\times \{1 + \tfrac{1}{2}a^2[1 + \Phi_2(\boldsymbol{x}, t)]\} - \Phi_1(\boldsymbol{x}, t).
\end{aligned}$$

Hence, if $Q(\boldsymbol{x}, t) = 0$, then $\mathcal{E}_+(\boldsymbol{x}, t) = \mathcal{E}_-(\boldsymbol{x}, t)$ also on the lattice. In this case the total lattice energy

$$E = \sum_{\boldsymbol{x} \in 2a\mathbb{Z}^D} \mathcal{E}_+(\boldsymbol{x}, t) \tag{2.10}$$

is exactly conserved in time, since it can also be written

$$E = \sum_{\boldsymbol{x} \in 2a(\mathbb{Z}+1/2)^D} \mathcal{E}_-(\boldsymbol{x}, t + a). \tag{2.11}$$

All this holds exactly on infinite space. If space is restricted to the (hyper)cube of side L, suitable boundary conditions on $\phi(\boldsymbol{x}, t)$ are necessary; PBC are of this type if $L = 2Na$ with N an integer.

In conclusion, we may regard $Q(\boldsymbol{x}, t) = 0$ as a discrete field equation which conserves the total energy E. Explicitly, $Q(\boldsymbol{x}, t) = 0$ reads

$$\begin{aligned}
\phi(\boldsymbol{x}, t + a) + \phi(\boldsymbol{x}, t - a) \\
= \frac{2^{1-D}\sum_{\boldsymbol{\sigma}}\phi(\boldsymbol{x} + a\boldsymbol{\sigma}, t)}{1 + \frac{1}{2}a^2[1 + 2^{-D}\sum_{\boldsymbol{\sigma}}\phi^2(\boldsymbol{x} + a\boldsymbol{\sigma}, t)]},
\end{aligned} \tag{2.12}$$

which evidently allows one to evolve in time any configuration known on two consecutive time slices, say $t = 0$ and $t = a$.

It is easy to check that $Q(\boldsymbol{x}, t) = 0$ indeed becomes Eq. (2.3) in the continuum $a \to 0$ limit. The order a^0 is trivially satisfied; odd powers of a vanish identically as a consequence of the symmetry of Eq. (2.12) under $a \to -a$, while the order a^2 produces Eq. (2.3).

Keeping up to $\mathcal{O}(a^4)$ in Eq. (2.12) yields

$$\ddot{\phi} - \nabla^2\phi + \phi + \phi^3 = a^2 Q_2 + \mathcal{O}(a^4),$$

$$Q_2 = -\frac{1}{2}(1+\phi^2)\nabla^2\phi - \frac{1}{12}\ddot{\ddot{\phi}} + \frac{1}{4}\Big[\nabla^2\nabla^2\phi - \frac{2}{3}\sum_{i=1}^{D}\frac{\partial^4\phi}{\partial x_i^4}\Big] - \phi[(\nabla\phi)^2 + \phi\nabla^2\phi]. \tag{2.13}$$

To cast Eq. (2.12) in a form suitable for numerical calculations, we define the lattice arrays $F(\boldsymbol{n}, s)$ and $G(\boldsymbol{n}, s)$ as

$$\begin{aligned} F(\boldsymbol{n}, s) &\equiv \phi(2\boldsymbol{n}a, 2sa), \\ G(\boldsymbol{n}, s) &\equiv \phi(2\boldsymbol{n}a - \boldsymbol{\sigma}_+ a, 2sa + a), \end{aligned} \tag{2.14}$$

where $\boldsymbol{n} \in \mathbb{Z}^D$, $s \in \mathbb{Z}$, and $\boldsymbol{\sigma}_+ \equiv (1, 1, , \ldots, 1)$.

We then obtain the iterative system

$$\begin{aligned} F(\boldsymbol{n}, s+1) &= -F(\boldsymbol{n}, s) + \frac{\sum_{\boldsymbol{\tau}} G(\boldsymbol{n}+\boldsymbol{\tau}, s)}{2^{D-1} + \frac{1}{4}a^2[2^D + \sum_{\boldsymbol{\tau}} G^2(\boldsymbol{n}+\boldsymbol{\tau}, s)]}, \\ G(\boldsymbol{n}, s+1) &= -G(\boldsymbol{n}, s) + \frac{\sum_{\boldsymbol{\tau}} F(\boldsymbol{n}-\boldsymbol{\tau}, s+1)}{2^{D-1} + \frac{1}{4}a^2[2^D + \sum_{\boldsymbol{\tau}} F^2(\boldsymbol{n}-\boldsymbol{\tau}, s+1)]}, \end{aligned} \tag{2.15}$$

where $\boldsymbol{\tau} = (\tau_1, \tau_2, \ldots, \tau_D)$, with $\tau_i = 0, 1$ and, according to the PBC, $F(\boldsymbol{n} + N\boldsymbol{\tau}, s) = F(\boldsymbol{n}, s)$ and $G(\boldsymbol{n} + N\boldsymbol{\tau}, s) = G(\boldsymbol{n}, s)$ for any $\boldsymbol{\tau}$.

As initial conditions we have to specify $F(\boldsymbol{n}, 0)$ and $G(\boldsymbol{n}, 0)$ for $0 \le n_i \le N-1$, $i = 1, 2, \ldots, D$. Once these values of the fields are provided, the iteration rules Eqs. (2.15) uniquely define $F(\boldsymbol{n}, s)$ and $G(\boldsymbol{n}, s)$ for all $s > 0$. A comparison of this discretized dynamics with other more traditional numerical treatments of hyperbolic partial differential equations was performed in $1+1$ dimensions [24]. Here we notice only that this approach is particularly efficient, stable, and accurate, especially when the continuum limit $a \to 0$ and very long evolution times are of interest.

All observables of the continuum can be rewritten on the lattice in terms of the basic fields $F(\boldsymbol{n}, s)$ and $G(\boldsymbol{n}, s)$, according to the correspondences rules Eqs. (2.8) and the identification Eq. (2.14). In the sequel, while referring to observables discretized as above, whenever possible we shall keep using the notation corresponding to continuum observables for simplicity. Particular care must be taken for ϕ^4, since its lattice definition in Eqs. (2.8) uses a product of fields over different lattice sizes. This is harmless in the continuum limit for smooth fields, but makes a difference for fields with large ultraviolet support, as we shall see shortly. For this reason, we shall keep the notation $\phi^4_{\pm}(\boldsymbol{x}, t)$ given in Eqs. (2.8) distinct from the ultralocal definition $\phi^4(\boldsymbol{x}, t) \equiv [\phi(\boldsymbol{x}, t)]^4$.

D. Averaged observables

The key observables in our investigation are the basic quantities

$$\phi, \ \phi^2, \ \phi^4, \ \dot{\phi}^2, \ (\nabla\phi)^2, \tag{2.16}$$

as well as the power spectra of ϕ and π, that is $|\tilde{\phi}_{\boldsymbol{k}}(t)|^2$ and $|\tilde{\pi}_{\boldsymbol{k}}(t)|^2$, where $\tilde{\phi}_{\boldsymbol{k}}(t)$ and $\tilde{\pi}_{\boldsymbol{k}}(t)$ are given by Eq. (2.5). Let us recall again that we are using here the continuum notation also for the Fourier transforms, although they actually are discrete Fourier transforms.

The fluctuations of all these observables do not vanish upon time evolution. Hence for generic initial conditions they do not have any limit as $t \to \infty$. These are fine-grained or microscopic observables. Typically there are several spatiotemporal scales: the microscopic scales correspond to very fast oscillations and short distance variations that are of no relevance to a thermodynamic description. We are interested in longer, macroscopic scales that describe the relaxation of observables towards a state of equilibrium.

In particular, the ergodic postulate states that ensemble averages must be identified with *long* time averages as well as spatial averages over macroscopic-sized regions. Hence to make contact between the time evolution and the thermal averages we need to properly average the microscopic fluctuations.

First of all, for local quantities such as those in Eq. (2.16) we take the spatial average. Secondly, we take suitable time averages of all key observables in the following way:

$$\overline{\phi^2}(t) \equiv \frac{1}{\tau}\int_{t-\tau}^{t} dt' \frac{1}{V}\int_V d^3x \phi^2(\boldsymbol{x}, t'), \tag{2.17}$$

where $\tau \gg a$ fixes a limit to our resolution power in time. τ need not be constant throughout the time evolution. For instance, we find that a practical and efficient choice is

$$\tau(t) = \tau(0) + Ct, \tag{2.18}$$

where C is small and positive with typical values ~ 0.1. In this way we still keep $t \gg \tau(t)$ while the dependence on the initial values becomes negligible for practically accessible times. This method is quite effective in revealing general features of the (logarithmic) time evolution such as the presence of distinct stages characterized by well-separated macroscopic time scales.

Besides the time average, for more detailed observables such as the power spectra we performed an average over the discrete directions in space as discussed in Appendix A. Moreover, we sometimes averaged also over several initial conditions. Altogether, we denote the results of all these coarse grainings simply with an overbar to avoid cluttering of notation. For example, assuming equiprobable initial conditions

$$\overline{\phi}^{\,2}(t) = \frac{1}{M}\sum_{i=1}^{M}\frac{1}{\tau}\int_{t-\tau}^{t} dt' \frac{1}{V}\int_V d^3x [\phi^2(\boldsymbol{x}, t')]^{(i)},$$

where the superscript (i) labels the M different choices of smooth initial conditions, all with the same energy density E/V. Likewise, recalling the wave-vectors quantization $\boldsymbol{k} = (2\pi/L)\boldsymbol{n}$, we have

$$\overline{|\tilde{\pi}_k|^2}(t) = \frac{1}{M}\sum_{i=1}^{M}\frac{1}{S_n}\sum_{\boldsymbol{n}}\theta(n \le |\boldsymbol{n}| < n+1) \times \frac{1}{\tau}\int_{t-\tau}^{t} dt' |\tilde{\pi}_{\boldsymbol{k}}^{(i)}(t')|^2, \tag{2.19}$$

where the discrete radial wave number k is the average $|\boldsymbol{k}|$ over the shell of all S_n wave vectors $\boldsymbol{k} = (2\pi/L)\boldsymbol{n}$ satisfying $n \le |\boldsymbol{n}| < n+1$ (see Appendix A for more details). Analogous expressions hold for ϕ, ϕ^2, ϕ^4, π^2, $(\nabla\phi)^2$, $|\tilde{\pi}_{\boldsymbol{k}}|^2$, and $|\tilde{\phi}_{\boldsymbol{k}}|^2$.

In particular, due to the linearity of these averages, we have the sum rules:

$$\int_{-\Lambda}^{+\Lambda}\frac{d^3k}{(2\pi)^3}\overline{|\tilde{\phi}_{\boldsymbol{k}}|^2}(t) = \overline{\phi^2}(t), \qquad \int_{-\Lambda}^{+\Lambda}\frac{d^3k}{(2\pi)^3}\overline{|\tilde{\pi}_{\boldsymbol{k}}|^2}(t) = \overline{\pi^2}(t), \tag{2.20}$$

where $\Lambda = \pi/(2a)$ is the UV cutoff on the lattice and we write the wave numbers as continuous although they are discrete in all actual calculations.

Finally, let us recall that the power spectra are just the Fourier transforms of space-averaged correlation functions. For instance,

$$\overline{|\tilde{\phi}_{\boldsymbol{k}}|^2}(t) = \int_V d^3x e^{-i\boldsymbol{k}\cdot\boldsymbol{x}}\overline{\phi\phi}(\boldsymbol{x}, t), \tag{2.21}$$

where, according to our general rules,

$$\overline{\phi\phi}(\boldsymbol{x}, t) = \frac{1}{M}\sum_{i=1}^{M}\frac{1}{\tau}\int_{t-\tau}^{t}dt'\frac{1}{V}\int_V d^3y\,\phi^{(i)}(\boldsymbol{y}, t')\phi^{(i)}(\boldsymbol{x}+\boldsymbol{y}, t').$$

III. THERMAL EQUILIBRIUM

We present in this section the basic properties of the ϕ^4 theory in thermal equilibrium. These results will be compared in the subsequent sections with the time averages in order to asses whether and how thermalization is approached.

A. General aspects

The thermal average of any physical quantity $\Theta = \Theta[\phi, \pi]$ in the canonical ensemble is written as

$$\langle\Theta[\pi, \phi]\rangle = \frac{\int\!\!\int D\phi D\pi e^{-\beta H[\pi,\phi]}\Theta[\phi, \pi]}{\int\!\!\int D\phi D\pi e^{-\beta H[\pi,\phi]}}, \tag{3.1}$$

where $\int\!\!\int D\phi D\pi$ stands for functional integration over the classical phase space and $\beta \equiv 1/T$ is the inverse (dimensionless) temperature in the dimensionless variables. In terms of the *physical* temperature, here defined as T_p, T is given by

$$T = \frac{1}{\beta} \equiv \frac{\lambda}{m}T_p. \tag{3.2}$$

As a consequence of the field redefinition available in the classical theory, the relevant variable for equilibrium thermodynamics is T. Therefore, for a fixed physical temperature T_p we see from Eq. (3.2) that the low temperature limit $T \ll 1$ corresponds to the weak coupling limit and/or $T_p \ll m$. This will be relevant in the analysis below.

Translation invariance (which is preserved by PBC) implies that averages of local observables $\Theta(\boldsymbol{x})$ which depend on π and ϕ only at one point $\boldsymbol{x}$, do not depend on $\boldsymbol{x}$, that is $\langle\Theta(\boldsymbol{x})\rangle = \langle\Theta(0)\rangle \equiv \langle\Theta\rangle$.

Furthermore, the fact that the Hamiltonian is the sum of a kinetic and a potential term [see Eq. (2.4)] entails that the average of observables which are of the form

$$\Theta[\phi, \pi] = \Theta_1[\phi]\Theta_2[\pi],$$

factorize as

$$\langle\Theta[\phi, \pi]\rangle = \langle\Theta_1[\phi]\rangle_\phi\langle\Theta_2[\pi]\rangle_\pi$$

with

$$\langle\Theta_1[\phi]\rangle_\phi = \frac{\int D\phi e^{-\beta\mathcal{V}[\phi]}\Theta_\phi[\phi]}{\int D\phi e^{-\beta\mathcal{V}[\phi]}}, \qquad \langle\Theta_2[\pi]\rangle_\pi = \frac{\int D\pi e^{-\beta\mathcal{T}[\pi]}\Theta_\pi[\pi]}{\int D\pi e^{-\beta T[\pi]}}.$$

Moreover, since the π integration is Gaussian and ultralocal, it can be performed quite easily in most cases, leaving the configurational integral over $\phi = \phi(\boldsymbol{x})$ for $\boldsymbol{x} \in V$ to be computed.

It follows from Eqs. (2.4) and (3.1) that the two-point correlation function of the canonical momentum $\pi(\boldsymbol{x})$ in the classical theory in equilibrium is given by

$$\langle\pi(\boldsymbol{x})\pi(\boldsymbol{x}')\rangle = T\delta(\boldsymbol{x}-\boldsymbol{x}'), \tag{3.3}$$

which leads to a flat power spectrum for π

$$\langle|\tilde{\pi}_{\boldsymbol{k}}|^2\rangle = T, \tag{3.4}$$

where we used the Fourier transform Eq. (2.5). This is of course a consequence of equipartition and gives a criterion to identify the temperature: the height of the flat region in the power spectrum of π if such a flat region shows up.

Equation (3.4) implies that $\langle\pi^2\rangle = T\delta(\boldsymbol{0})$ where $\delta(\boldsymbol{0})$ is to be understood as made finite by some UV cutoff procedure. If a rotationally invariant sharp cutoff $\bar{\Lambda}$ is used, then $\delta(\boldsymbol{0}) = \bar{\Lambda}^3/(6\pi^2)$. In case of the lattice regularization of Sec. II B, with $\pi(\boldsymbol{x})$ entering only in the kinetic energy converted to a sum as in Eq. (2.6), we have instead $\delta(\boldsymbol{0}) = 1/(2a)^3$. Thus,

$$\langle \pi^2 \rangle^{(\text{sharp } \bar{\Lambda})} = \frac{T\bar{\Lambda}^3}{6\pi^2}, \qquad \langle \pi^2 \rangle^{(\text{lattice}, 2a)} = \frac{T}{(2a)^3}. \quad (3.5)$$

Equating these two regularized averages would yield the identification $\bar{\Lambda} = (6/\pi)^{1/3}(2\pi/a) = (6/\pi)^{1/3}\Lambda$; this connection between cutoffs is however not universal; it is valid only for $\langle \pi^2 \rangle$ and in general different for other UV-divergent quantities. Moreover, we will see below that the discretized dynamics described in Sec. II C provides a slightly different UV regularization even for $\langle |\tilde{\pi}_{\boldsymbol{k}}|^2 \rangle$.

At equilibrium, the classical virial theorem takes the form

$$\langle \dot{\phi}^2 \rangle = \langle (\nabla \phi)^2 \rangle + \langle \phi^2 \rangle + \langle \phi^4 \rangle, \quad (3.6)$$

where we have trivially generalized to three spatial dimensions the derivation in Ref. [9]. When combined with the energy functional $H[\pi, \phi]$ given in Eq. (2.4), it yields

$$\frac{\langle H[\pi, \phi] \rangle}{V} = \frac{E}{V} = \langle \pi^2 \rangle - \frac{1}{4}\langle \phi^4 \rangle, \quad (3.7)$$

where E is the average energy in the canonical ensemble. Since $N = V/(2a)^3$ is the total number of degrees of freedom in the simplest lattice regularization, we find using Eq. (3.5) that the temperature T is related to the (average) energy per degree of freedom as

$$T = \frac{E}{N} + 2a^3 \langle \phi^4 \rangle. \quad (3.8)$$

Therefore, for $a \ll 1$, close to the continuum limit where one finds $a^2\langle \phi^4 \rangle$ to be finite as $a \to 0$ (see below), the temperature is identified with the energy per site. Furthermore,

$$T = (2a)^3[\rho + \tfrac{1}{4}\langle \phi^4 \rangle], \quad (3.9)$$

where $\rho \equiv E/V$ is the energy density, while the pressure p is given in general (not necessarily at thermal equilibrium) by

$$p = \tfrac{1}{2}[\dot{\phi}^2 - \tfrac{1}{3}(\nabla \phi)^2 - \phi^2 - \tfrac{1}{2}\phi^4]. \quad (3.10)$$

At thermal equilibrium we find from Eqs. (3.6), (3.9), and (3.10) the equation of state

$$\langle p \rangle = \tfrac{1}{3}\rho - \tfrac{1}{3}\langle \phi^2 \rangle \quad (3.11)$$

that is a radiation-dominated equation of state $\langle p \rangle \simeq \rho/3$, since $\langle \phi^2 \rangle$ is of order a^{-1}, much smaller than $\langle p \rangle$ and ρ which are both of order a^{-3} for fixed T.

B. Perturbation theory, Hartree resummation and beyond

The continuum configurational functional integrals

$$\langle \Theta[\phi] \rangle = \frac{\int D\phi e^{-\beta V[\phi]} \Theta[\phi]}{\int D\phi e^{-\beta V[\phi]}} \quad (3.12)$$

can be computed in a perturbative expansion in powers of T. In order to do that one changes the functional integration variable $\phi(\boldsymbol{x})$ to

$$\chi(\boldsymbol{x}) \equiv \frac{1}{\sqrt{T}}\phi(\boldsymbol{x}).$$

Equation (3.12) takes thus the form

$$\langle \Theta[\phi] \rangle = \frac{\int D\chi e^{-1/2 \int d^3x [(\nabla\chi)^2 + \chi^2 + (T/2)\chi^4]} \Theta[\sqrt{T}\chi]}{\int D\chi e^{-1/2 \int d^3x [(\nabla\chi)^2 + \chi^2 + (T/2)\chi^4]}}. \quad (3.13)$$

We read from Eq. (3.13) the associate Feynman rules. The Euclidean χ propagator in three space dimensions takes in momentum space the form

$$\Delta_\chi = \frac{1}{k^2 + 1},$$

and the quadrilinear χ vertex has $(-6T)$ as a coefficient.

As already recalled above, this defines a superrenormalizable field theory with only two divergent diagrams: the one-loop tadpole and the two-loop sunset. Recall that in classical statistical mechanics the regularized (bare) theory is the physical one. The ultraviolet divergences are physical and cannot be eliminated by counterterms as in quantum field theory.

The two-point function $\langle \phi(\boldsymbol{x})\phi(\boldsymbol{x}') \rangle$ can be written as

$$\langle \phi(\boldsymbol{x})\phi(\boldsymbol{x}') \rangle = \int \frac{d^3k}{(2\pi)^3} \langle |\tilde{\phi}_{\boldsymbol{k}}|^2 \rangle e^{i\boldsymbol{k}\cdot(\boldsymbol{x}-\boldsymbol{x}')},$$
$$\langle |\tilde{\phi}_{\boldsymbol{k}}|^2 \rangle = \frac{T}{k^2 + 1 + \Sigma(k^2)}, \quad (3.14)$$

where $\Sigma(k^2)$ stands for the self-energy.

To lowest order in T the tadpole takes then the form

$$\langle \phi^2 \rangle = T \int_{k<\bar{\Lambda}} \frac{d^3k}{(2\pi)^3} \frac{1}{k^2 + 1} \overset{\bar{\Lambda} \gg 1}{=} \frac{T\bar{\Lambda}}{2\pi^2}[1 + \mathcal{O}(\bar{\Lambda}^{-1})], \quad (3.15)$$

while the self-energy reads to lowest order

$$\Sigma = 3\langle \phi^2 \rangle \overset{\bar{\Lambda} \gg 1}{=} \frac{3T\bar{\Lambda}}{2\pi^2}[1 + \mathcal{O}(\bar{\Lambda}^{-1})].$$

Here we are using the sharp spherically symmetric UV cutoff, to be compared later on to the lattice regularization method with cutoff $\Lambda = \pi/(2a)$.

To next order Σ contains the two-loop sunset diagram, which is only logarithmically divergent; therefore the tadpole dominates the effective mass in the limit $\bar{\Lambda} \to \infty$. Hence, in this limit the two-point function is dominated by the Hartree approximation (the sum of all daisy diagrams)

$$\langle |\tilde{\phi}_{\boldsymbol{k}}|^2 \rangle \simeq \frac{T}{k^2 + 1 + 3\langle \phi^2 \rangle}, \quad (3.16)$$

where the self-consistent $\langle \phi^2 \rangle$ fulfills

$$\langle\phi^2\rangle = \int \frac{d^3k}{(2\pi)^3}\langle|\tilde{\phi}_{\boldsymbol{k}}|^2\rangle = \int \frac{d^3k}{(2\pi)^3}\,\frac{T}{k^2+1+3\langle\phi^2\rangle} \simeq \frac{T}{2\pi^2}\left[\bar{\Lambda} - \sqrt{\tfrac{3}{8}T\bar{\Lambda}} + \cdots\right]. \tag{3.17}$$

We analogously find for the gradient squared $(\nabla\phi)^2$, at lowest order

$$\langle(\nabla\phi)^2\rangle = \frac{T}{12\pi}\left(\bar{\Lambda}^2 - \frac{6}{\pi^2}\bar{\Lambda}\right) + \mathcal{O}(\bar{\Lambda}^0), \tag{3.18}$$

and for $\langle\phi^4\rangle$ using Wick's theorem,

$$\langle\phi^4\rangle = 3\langle\phi^2\rangle^2[1+\mathcal{O}(\bar{\Lambda}^{-1})] = \frac{3T^2}{4\pi^4}[\bar{\Lambda}^2 + \mathcal{O}(\bar{\Lambda})]. \tag{3.19}$$

By construction, the Hartree resummation does not change the first order result $\langle\phi^4\rangle = 3\langle\phi^2\rangle^2$. One may also check that it provides the correct next-to-leading term of order $\sqrt{\bar{\Lambda}}$ to $\langle\phi^4\rangle/\bar{\Lambda}^2$, since the first, three-loop divergent diagram not of a daisy type is only linearly divergent.

Beyond the Hartree approximation the self-energy $\Sigma(k^2)$ receives a k-independent logarithmically diverging contribution (from the sunset diagram with dressed propagators) plus a k-dependent UV finite contribution. All these corrections can be conveniently parametrized through a suitable function $Z(k^2)$ by writing

$$\langle|\tilde{\phi}_{\boldsymbol{k}}|^2\rangle = \frac{TZ(k^2)}{k^2+1+3\langle\phi^2\rangle}, \tag{3.20}$$

where $\langle\phi^2\rangle$ is now the exact expectation value and $Z(k^2)$ is of course a function also of T and of the UV cutoff $\bar{\Lambda}$, that is $Z(k^2) = Z(k^2; T, \bar{\Lambda})$.[1] By construction $Z(k^2; T, \bar{\Lambda})$ depends at most logarithmically on the cutoff.

We have from Eqs. (3.14) and (3.20),

$$\frac{1}{Z(k^2)} = \frac{k^2+1+\Sigma(k^2)}{k^2+1+3\langle\phi^2\rangle} = 1 + \frac{\tilde{\Sigma}(k^2)}{k^2+M^2},$$

where $M^2 = 1+3\langle\phi^2\rangle$ and $\tilde{\Sigma}(k^2) = \Sigma(k^2) - 3\langle\phi^2\rangle$. Notice that $\tilde{\Sigma}(k^2)$ can also be written as a sum of Feynman diagrams with dressed propagators $(k^2+M^2)^{-1}$ and no tadpole insertion of any order. Thus, the lowest order contribution to $\tilde{\Sigma}(k^2)$ comes from the sunset diagrams with dressed propagators. Now, since the renormalized ϕ^4 QFT is asymptotically free in the ultraviolet (that is the ultraviolet is controlled by the Gaussian fixed point), the exact ϕ two-point function must behave as $1/k^2$ in the ultraviolet (even in the presence of the cutoff $\bar{\Lambda}$, provided k remains much smaller than $\bar{\Lambda}$). Thus we expect $Z(k^2)$ to tend to unity for large k (and from above, since the two-loop sunset diagram enters in $\tilde{\Sigma}$ with a minus sign), while $\langle\phi^2\rangle$ still diverges linearly with $\bar{\Lambda}$. Since the only divergence in $\tilde{\Sigma}(k^2)$ comes from the sunset diagrams and is only logarithmic, $Z(k^2; T, \bar{\Lambda})$ tends to 1 for all k in the limit $\bar{\Lambda}\to\infty$ to any finite order of perturbation theory. A different behavior in $\bar{\Lambda}$ would signal a nonperturbative effect.

To know more about $Z(k^2)$, in a nonperturbative way, we resort to Monte Carlo simulations in Sec. III D. In preparation, we need to reexpress some relevant equilibrium quantities with the lattice regularization which corresponds to the discrete dynamics of Sec. II C.

C. Equilibrium on the lattice

Thermal expectation values on the lattice are written as their continuum counterparts, Eq. (3.1), in terms of standard multiple integrals over phase-space degrees of freedom and the statistical weight $\exp(-H/T)$ where H is now the lattice Hamiltonian. As phase-space degrees of freedom we take $\pi_+(\boldsymbol{x}, 0) \equiv \pi_+(\boldsymbol{x})$ and $\phi(\boldsymbol{x}+a\boldsymbol{\sigma}_+, 0) \equiv \phi(\boldsymbol{x}+a\boldsymbol{\sigma}_+)$ with $\boldsymbol{x}\in 2a\mathbb{Z}^3$, or better $\boldsymbol{x}\in 2aC_N$ after the restriction to a finite volume (see Sec. II B). As a lattice Hamiltonian we take the total conserved energy of Eqs. (2.9) and (2.10) with $D=3$, namely,

$$\begin{aligned} H[\pi_+, \phi] &= \sum_{\boldsymbol{x}\in 2aC_N} \mathcal{E}_+(\boldsymbol{x}, 0) \\ &= \frac{1}{2}\sum_{\boldsymbol{x}}(2a)^3\left[\pi_+^2 + (D\phi)^2 + \phi_+^2 + \frac{1}{2}\phi_+^4\right] \\ &= \frac{1}{2}\sum_{\boldsymbol{x}}(2a)^3\left[\pi_+^2 + (D\phi)^2 + \frac{1}{2}\Phi^{(2)}\right. \\ &\quad \left. + \frac{1}{2}(\Phi^{(1)} + a\pi_+)^2(1+\Phi^{(2)})\right], \end{aligned} \tag{3.21}$$

where we used the first of Eqs. (2.8) to express $\phi(\boldsymbol{x}, a)$ as $\Phi^{(1)}(\boldsymbol{x}, 0) + a\pi_+(\boldsymbol{x}, 0)$. We see that the momentum field π_+ enters the lattice Hamiltonian in a way definitely more involved than in the continuum, Eq. (2.4), or in the naive lattice regularization where only space is discretized and π enters only the kinetic energy as in Eq. (2.6). However, $H[\pi_+, \phi]$ still depends on π_+ only ultralocally, so that π_+ plays the role of a Gaussian auxiliary field which could be integrated away to produce an effective Hamiltonian for ϕ alone with a nonpolynomial local self-interaction. This self-interaction reproduces the standard continuum ϕ^4 potential $\mathcal{V}[\phi]$ in the limit $a\to 0$. However, it is simpler not to integrate over π_+ and keep working with the quartic Hamiltonian Eq. (3.21).

We discuss first the Gaussian approximation to the thermal equilibrium on the lattice. This is valid for the linearization around classical solutions (zero field and the cnoidal) as well as for the self-consistent Hartree approximation.

[1] Here $\bar{\Lambda}$ need not be a sharp cutoff as in the lowest perturbative order or in the Hartree approximation; our only request is that it is the UV cutoff in some spherically symmetric regularization procedure. For instance, one could use free-field propagators smeared in the ultraviolet by some smooth function of $k/\bar{\Lambda}$ dying at infinity faster than any power.

Consider the lattice equation of motion (2.12) and the first of the correspondence rules Eq. (2.8) written in Fourier space, that is

$$\tilde{\pi}_{\pm,\boldsymbol{k}}(t) = \pm\frac{1}{a}[\tilde{\phi}_{\boldsymbol{k}}(t \pm a) - \tilde{\phi}_{\boldsymbol{k}}(t)],$$
$$C(\boldsymbol{k}a) \equiv \prod_{j=1}^{D} \cos k_j a. \tag{3.22}$$

Next we take the free-field limit of Eq. (2.12) by linearizing it. Details are reported in Appendix B, where linearization is performed more generally over the uniform time-dependent solution of the discrete dynamics (the discrete cnoidal). Free-field dynamics is decoupled in Fourier space and the harmonic also on the lattice, so that the standard virial theorem for harmonic oscillations (which holds true for phase-space averages as well as for time averages) yields, as in Eq. (B6) specialized to $D = 3$,

$$\langle|\tilde{\phi}_{\boldsymbol{k}}|^2\rangle = a^2\Big[1 - \frac{1-\frac{1}{2}a^2}{1+\frac{1}{2}a^2}C(\boldsymbol{k}a)\Big]^{-1}\langle|\tilde{\pi}_{+,\boldsymbol{k}}|^2\rangle$$
$$= \frac{a^2 T}{[1+\frac{1}{2}a^2 - (1-\frac{1}{2}a^2)C^2(\boldsymbol{k}a)]} \equiv G_0(\boldsymbol{k}, a) \tag{3.23}$$

having used equipartition, that is $\langle|\tilde{\pi}_{+,\boldsymbol{k}}|^2\rangle = T/(1+\frac{1}{2}a^2)$, as follows from the quadratic part of the Hamiltonian Eq. (3.21). $G_0(\boldsymbol{k}, a)$ in Eq. (3.23) is the tree level (Fourier transform) of the ϕ two-point function on the lattice and can be seen to coincide with the result obtained by integrating π_+ away within a quadratic approximation. Notice that $\langle|\tilde{\phi}_{\boldsymbol{0}}|^2\rangle = 1$ as its continuum counterpart. The small a-dependent tree-level correction in $\langle|\tilde{\pi}_{+,\boldsymbol{k}}|^2\rangle = T/(1+\frac{1}{2}a^2)$ with respect to the continuum $\langle|\tilde{\pi}_{\boldsymbol{k}}|^2\rangle = T$ is evidently a first effect of our specific lattice regularization. Similarly, the finite lattice version of the tree-level tadpole reads

$$\langle\phi^2\rangle = \frac{1}{L^3}\sum_{\boldsymbol{k}\in(2\pi/L)C_N} G_0(\boldsymbol{k}, a) \overset{L\to\infty}{=} \frac{T}{a}[1 + \mathcal{O}(a)]$$
$$\times \int_{-\pi/2}^{+\pi/2}\frac{d^3q}{(2\pi)^3}\,\frac{1}{1-C^2(\boldsymbol{q})}$$
$$= 0.1741\cdots\frac{T}{a}[1 + \mathcal{O}(a)]$$
$$= 0.1108\cdots T\Lambda[1 + \mathcal{O}(\Lambda^{-1})] \tag{3.24}$$

to be compared with the infinite-volume continuum expression Eq. (3.15). If these two expressions are identified, one obtains the tree-level relation $\bar{\Lambda} = 2.187\cdots\Lambda$, which differs from that implied by $\langle\pi^2\rangle$ (see Sec. III A).

Another important issue about lattice effects concerns the equilibrium expectation value of ϕ^4. We have already commented at the end of Sec. II C on two different lattice regularizations of ϕ^4, the slightly nonlocal $\phi^4_\pm$ of Eqs. (2.8) and the ultralocal $\phi^4(\boldsymbol{x}) \equiv [\phi(\boldsymbol{x})]^4$. They do not yield the same values due to ultraviolet effects. At equilibrium this appears quite evident already at tree level: the application of the Wick theorem to the expectation value of the ultralocal ϕ^4 yields

$$\langle\phi^4\rangle = 3\langle\phi^2\rangle^2, \qquad \langle\phi^2\rangle = \frac{1}{V}\sum_{\boldsymbol{k}} G_0(\boldsymbol{k}, a)$$

as in the continuum, only with a sum over wave vectors in the first Brillouin zone rather than a rotation invariant integral as in Sec. III B. The same Wick rules on Gaussian integration plus translation invariance give instead for ϕ^4_+

$$\langle\phi^4_+\rangle = \langle(\Phi^{(1)} + a\pi_+)^2\Phi^{(2)}\rangle$$
$$= \frac{T\langle\Phi^{(2)}\rangle}{8a(1+\frac{1}{2}a^2)} + \frac{\langle[\Phi^{(1)}]^2\Phi^{(2)}\rangle}{(1+\frac{1}{2}a^2)^2}$$
$$= \frac{\langle\phi^2\rangle}{1+\frac{1}{2}a^2}\Big[\frac{T}{8a} + \frac{I_2}{1+\frac{1}{2}a^2}\Big] + \frac{2I_2^2}{(1+\frac{1}{2}a^2)^2},$$
$$I_2 \equiv \frac{1}{V}\sum_{\boldsymbol{k}} C^2(\boldsymbol{k}a)G_0(\boldsymbol{k}, a).$$

A straightforward numerical integration yields the tree-level ratio

$$\langle\phi^4_+\rangle/\langle\phi^2\rangle^2 = 1.154\,748\cdots \tag{3.25}$$

for $L = 12.8$ and $a = 0.0125$.

When the interaction is turned on both $\langle|\tilde{\pi}_{+,\boldsymbol{k}}|^2\rangle$ and $\langle|\tilde{\phi}_{\boldsymbol{k}}|^2\rangle$ gets modified. The relations between $\langle|\tilde{\pi}_{+,\boldsymbol{k}}|^2\rangle$ and the temperature T get new corrections in terms of expectation values of ϕ-dependent observables. A look at Eq. (3.21), with the knowledge that the Euclidean ϕ^4 QFT is superrenormalizable (so that UV divergences can be fully assessed from perturbation theory as in the previous section), reveals that these corrections all vanish at least linearly as $a \to 0$, so that the continuum result $\langle|\tilde{\pi}_{\boldsymbol{k}}|^2\rangle = T$ is recovered. At any rate, here we are only seeking a convenient parametrization for $\langle|\tilde{\phi}_{\boldsymbol{k}}|^2\rangle$ in terms of $\langle|\tilde{\pi}_{+,\boldsymbol{k}}|^2\rangle$ and $\langle\phi^2\rangle$.

Again, we may resort to the linearization of the discrete equation of motion, this time over a uniform nonzero background $\phi(t)$, as detailed in Appendix B. First of all we learn how to obtain the Hartree resummation on the lattice: we replace the background $\phi^2(t)$ with the equilibrium expectation value $\langle\phi^2\rangle$ in the dispersion relation Eq. (B4), obtaining

$$\cos[\omega_{\boldsymbol{k}}a] = B(\langle\phi^2\rangle)C(\boldsymbol{k}a),$$
$$B(u) = \frac{1+\frac{1}{2}a^2(1-u)}{[1+\frac{1}{2}a^2(1+u)]^2} \tag{3.26}$$

and invoke the virial theorem (the Hartree approximation is Gaussian, that is it describes harmonic oscillations) to write

$$\langle|\tilde{\phi}_{\boldsymbol{k}}|^2\rangle = \frac{a^2\langle|\tilde{\pi}_{+,\boldsymbol{k}}|^2\rangle}{1-(1-\frac{1}{4}a^4)\cos^2\omega_{\boldsymbol{k}}a} \simeq \frac{a^2\langle|\tilde{\pi}_{+,\boldsymbol{k}}|^2\rangle}{1-[B(\langle\phi^2\rangle)C(\boldsymbol{k}a)]^2}. \tag{3.27}$$

We have neglected the term $a^4\cos^2\omega_{\boldsymbol{k}}$ in the last step since it is of order a^4 for all $\boldsymbol{k}$. Beyond the Hartree approximation, we promote Eq. (3.27) to an exact relation by introducing the k-dependent lattice analog of $Z(k^2)$; that is $Z_{\boldsymbol{k}} = Z_{\boldsymbol{k}}(T, a)$

$$\langle|\tilde{\phi}_{\boldsymbol{k}}|^2\rangle = \frac{a^2 Z_{\boldsymbol{k}}\langle|\tilde{\pi}_{+,\boldsymbol{k}}|^2\rangle}{1-[B(\langle\phi^2\rangle)C(\boldsymbol{k}a)]^2}, \qquad Z_{\boldsymbol{k}} \stackrel{\text{def}}{=} \frac{1-[B(\langle\phi^2\rangle)C(\boldsymbol{k}a)]^2}{a^2\langle|\tilde{\pi}_{+,\boldsymbol{k}}|^2\rangle}\langle|\tilde{\phi}_{\boldsymbol{k}}|^2\rangle. \tag{3.28}$$

By construction $Z_{\boldsymbol{k}}(T, a)$ is as much as possible free from lattice effects (such as the deformation of the free-field propagator at large $|\boldsymbol{k}|$ due to the replacement of continuum derivatives with finite differences) and, once averaged over discrete directions to $Z_k(T, a)$, it should provide a rather accurate representation of its continuum counterpart $Z(k^2; T, \bar{\Lambda})$, if a universal relation between $\bar{\Lambda}$ and $\Lambda = \pi/(2a)$ could be determined. As we have seen above, in the case of UV-divergent quantities like $\langle\pi^2\rangle$ and $\langle\phi^2\rangle$ this is not possible, but should be possible for renormalized or UV finite observables. Perturbation theory suggests this to be the case for $Z(k^2; T, \bar{\Lambda})$. In the next section we shall follow a different, nonperturbative strategy, based on the simple observation that the agreement of lattice calculations with their continuum $\bar{\Lambda}$-cutoffed counterparts is guaranteed for all observables in a different limit; that is $\Lambda \to \infty$ first, at fixed large $\bar{\Lambda}$, rather than Λ, $\bar{\Lambda} \to \infty$ with $\Lambda = \mathcal{O}(\bar{\Lambda})$. For $\boldsymbol{k}$-dependent quantities this means agreement for $|\boldsymbol{k}| \lesssim \bar{\Lambda} \ll \Lambda$.

D. Monte Carlo simulations

Monte Carlo simulations allow one to compute thermodynamical averages beyond perturbation theory and Hartree resummation. We performed Metropolis simulations for the ϕ^4 model discretized on the lattice as in Sec. II C.

Consider the lattice Hamiltonian $H[\pi_+, \phi]$ of Eq. (3.21). In this context it is more convenient to revert to the notation with the single field ϕ, using both $\phi(\boldsymbol{x}, 0)$ and $\phi(\boldsymbol{x}, a)$. We may drop the distinction between the two time slices by considering the degrees of freedom attached to a cell-centered cubic lattice. There are therefore the points of $2a\mathbb{Z}^3$, labeled by $\boldsymbol{x} = 2a\boldsymbol{n}$, $\boldsymbol{n}$ having integer coordinates, and the points of $2a(\mathbb{Z}+1/2)^3$ labeled $\boldsymbol{x} + a\boldsymbol{\sigma}_+$, where $\boldsymbol{\sigma}_+ = (1, 1, 1)$. The Hamiltonian can then be written as

$$H = 2a(2+a^2)\sum_{\boldsymbol{x}\in 2a\mathbb{Z}^3}[\phi^2(\boldsymbol{x}) + \phi^2(\boldsymbol{x}+a\boldsymbol{\sigma}_+)] - a\sum_{\boldsymbol{x}\in 2a\mathbb{Z}^3}\sum_{\boldsymbol{\sigma}}\phi(\boldsymbol{x})\phi(\boldsymbol{x}+a\boldsymbol{\sigma}) \times\left[1-\frac{1}{4}a^2\phi(\boldsymbol{x})\phi(\boldsymbol{x}+a\boldsymbol{\sigma})\right]. \tag{3.29}$$

This Hamiltonian contains local terms and couplings between nearest neighbors along the main diagonals. The quartic term contributes to these couplings and there is no quartic local term. However, to perform Monte Carlo simulations is more convenient to add and subtract a quartic local piece. In this way one can change the local integration variables $-\infty < \phi(\boldsymbol{x}) < +\infty$ in Eq. (3.1) to a new variable $C(\boldsymbol{x})$ ranging from zero to 1 as in [25].

We therefore split our Hamiltonian Eq. (3.29) as

$$H = H_1 + H_2,$$
$$H_1 = \sum_{\boldsymbol{x}\in 2a\mathbb{Z}^3}\{h_1[\phi(\boldsymbol{x})] + h_1[\phi(\boldsymbol{x}+a\boldsymbol{\sigma}_+)]\},$$
$$h_1[\phi] \equiv 4a(2+a^2)\phi^2 + 2a^3\phi^4,$$
$$H_2 = -a\sum_{\boldsymbol{x}\in 2a\mathbb{Z}^3}\sum_{\boldsymbol{\sigma}}\phi(\boldsymbol{x})\phi(\boldsymbol{x}+a\boldsymbol{\sigma}) + \frac{a^3}{4}\sum_{\boldsymbol{x}\in 2a\mathbb{Z}^3}\sum_{\boldsymbol{\sigma}}\phi^2(\boldsymbol{x}) \times[\phi^2(\boldsymbol{x}+a\boldsymbol{\sigma}) - \phi^2(\boldsymbol{x})]. \tag{3.30}$$

The functional integral in Eq. (3.1) can be written as

$$\langle\Theta\rangle = \frac{\int_\infty^{+\infty}\cdots\int_{-\infty}^{+\infty}[\prod_{\boldsymbol{x}} d\phi(\boldsymbol{x}) e^{-\beta h_1[\phi(\boldsymbol{x})]}]\Theta[\phi(\cdot)]e^{-\beta H_2[\phi(\cdot)]}}{\int_\infty^{+\infty}\cdots\int_{-\infty}^{+\infty}[\prod_{\boldsymbol{x}} d\phi(\boldsymbol{x}) e^{-\beta h_1[\phi(\boldsymbol{x})]}]e^{-\beta H_2[\phi(\cdot)]}} = \frac{\int_0^1\cdots\int_0^1[\prod_{\boldsymbol{x}} dC(\boldsymbol{x})]\Theta[C(\cdot)]e^{-\beta H_2[C(\cdot)]}}{\int_0^1\cdots\int_0^1[\prod_{\boldsymbol{x}} dC(\boldsymbol{x})]e^{-\beta H_2[C(\cdot)]}}, \tag{3.31}$$

where the new field C is defined as

$$C(\phi) \equiv = \frac{\int_{-\infty}^{\phi} dx e^{-\beta h_1[x]}}{\int_{-\infty}^{+\infty} dx e^{-\beta h_1[x]}}. \tag{3.32}$$

In this way the classical ϕ^4 model is mapped into a classical continuous Ising-like model where the dynamical variables $C(\boldsymbol{x})$ run between zero and 1. The Ising-like Hamiltonian is given by H_2 [Eq. (3.30)].

Following the Metropolis method we generate a sequence of configurations for the whole cell-centered cubic lattice, as follows. We start by choosing random values at each point of the lattice for the variables $C(\boldsymbol{x})$. Then, we choose one point in the lattice $\boldsymbol{x}$ at random and consider a new value C' for it picked at random between zero and 1. We then have to go back from the variables $C(\boldsymbol{x})$ to the variables $\phi(\boldsymbol{x})$ in order to compute the energy of the old and new configurations. Notice that the inverse function $\phi = \phi(C)$ is unique since $dC/d\phi > 0$ as one sees from Eq. (3.32). Their energy change is given by

$$\Delta \equiv H_2(\text{new}) - H_2(\text{old})$$
$$= 2a[\phi' - \phi(\boldsymbol{x})]\Big\{\sum_{\boldsymbol{\sigma}} \phi^2(\boldsymbol{x} + a\boldsymbol{\sigma}) - 4[\phi'^2 + \phi^2(\boldsymbol{x})]\Big\},$$

where we used Eq. (3.30) and $\phi' \equiv \phi(C')$.

We now follow the standard Metropolis procedure. That is, we compare $e^{-\beta\Delta}$ with a random number r with $0 < r < 1$. If $r < e^{-\beta\Delta}$ we pick the new configuration. Otherwise, for $r > e^{-\beta\Delta}$ we keep the old one. We repeat this process many times producing in this way a sequence of configurations on which we can compute the values of any observable Θ.

It can be shown [25] that the average of these values of Θ converges to the thermodynamical phase average in the limit when the number of iterations $\mathcal{N}$ goes to infinity The expectation value is then given by

$$\langle\Theta\rangle = \frac{1}{\mathcal{N}} \sum_{n=1}^{\mathcal{N}} \Theta_n.$$

In the continuous limit $a \to 0$ we see from Eq. (3.30) that the quartic terms become negligible and hence all quantities will be functions of $\beta a = a/T$. In addition, gradients of the fields scale as $1/a$.

In Fig. 1 we plot $\langle\phi^2\rangle$, $\langle(\nabla\phi)^2\rangle$, and the ratio $\langle\phi^4\rangle/[\langle\phi^2\rangle]^2$ as functions of T/a from Monte Carlo simulations. We see that $\langle\phi^2\rangle$ and $\langle(\nabla\phi)^2\rangle$ follow the linear behavior predicted by low temperature perturbation theory Eq. (3.15) while the ratio $\langle\phi^4\rangle/[\langle\phi^2\rangle]^2$ takes the value 3 predicted by Wick's theorem in low temperature perturbation theory Eq. (3.19) or in Hartree approximation. As for the nonlocal lattice version of ϕ^4, that is ϕ^4_+, we find from the Monte Carlo simulations $\langle\phi^4_+\rangle/[\langle\phi^2\rangle]^2 \simeq 1.1\cdots$ for $a = 0.05$ and $L = 3.2$ in agreement with Eq. (3.25).

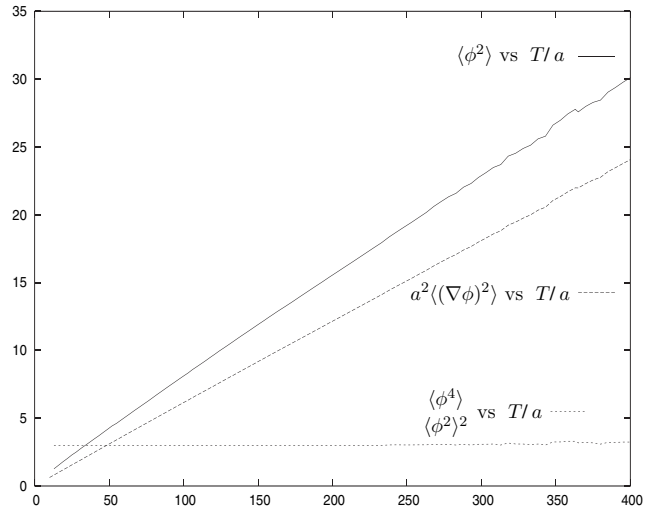

FIG. 1. $\langle\phi^2\rangle$, $\langle(\nabla\phi)^2\rangle$, and the ratio $\langle\phi^4\rangle/\langle\phi^2\rangle^2$ as a function of T/a in thermal equilibrium from Monte Carlo simulations.

As a matter of fact, by measuring also the two-point function $\langle\phi(\boldsymbol{x})\phi(\boldsymbol{x}')\rangle$, we verified that the Hartree approximation is indeed quite accurate for a very wide range of wavelengths which extends to the ultraviolet (this explains why UV-divergent quantities like $\langle\phi^2\rangle$, $\langle(\nabla\phi)^2\rangle$, and $\langle\phi^4\rangle$ are well approximated by Hartree). This is apparent from Fig. 2 which shows an almost perfect linear behavior of the inverse (of the direction-averaged) ϕ power spectrum, $1/\langle|\tilde{\phi}_{\boldsymbol{k}}|^2\rangle$, as a function of the lattice-artifact corrected k^2 which includes also the Hartree contribution to the mass, that is $a^{-2}[1 - [B(\langle\phi^2\rangle)C(\boldsymbol{k}a)]^2]$ (see previous section). The behavior seems linear also at small wave numbers (see the inset in the same figure), but the overall large scale does not allow one to appreciate a small but important deviation from linearity at small k^2.

This deviation is much better visible if we plot Z_k vs k instead. Now the accuracy of the Hartree approximation is evident in the rapid drop of Z_k to unity as k grows, while at small k we observe a significant deviation of $Z(k^2)$ from unity, with values of $Z(k^2) - 1$ of order 1 on lattices with lattice spacings down to $a = 0.0125$ and for temperatures of order 1. As an example, in the upper part of Fig. 3 we plot Z_k, the average over directions of $Z_{\boldsymbol{k}}$ defined by Eq. (3.28), versus the radial wave number k, for $T = 0.343$ and $a = 0.0125$. In the lower part we plot the (direction-averaged) π power spectrum $\overline{|\tilde{\pi}_k|^2}(t)$ to check that it is indeed almost constant and very close to its continuum limit $T = 0.343$.

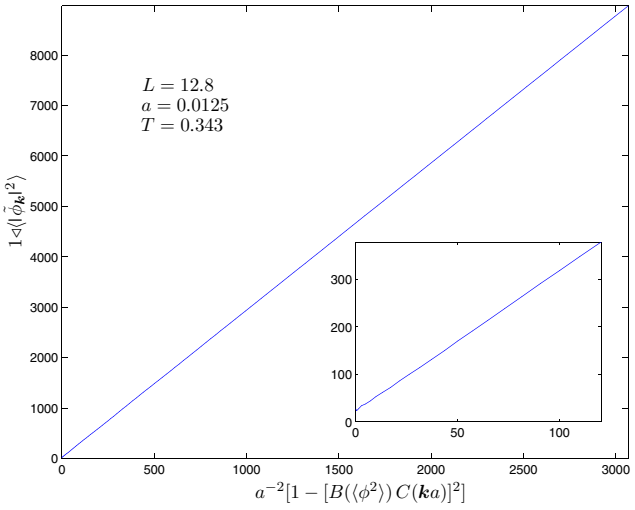

FIG. 2 (color online). $1/\langle|\tilde{\phi}_{\boldsymbol{k}}|^2\rangle$, the inverse of the direction-averaged ϕ power spectrum, as a function of $a^{-2}[1 - [B(\langle\phi^2\rangle)C(\boldsymbol{k}a)]^2]$, which reproduces $k^2 + 1 + 3\langle\phi^2\rangle$ for small ka while including the lattice artifacts when ka becomes of order 1. In the present case the UV cutoff is $\Lambda = 125.6637$. The almost linear behavior of $1/\langle|\tilde{\phi}_{\boldsymbol{k}}|^2\rangle$ down to relatively small ka (see the inset) supports the accuracy of the Hartree approximation.

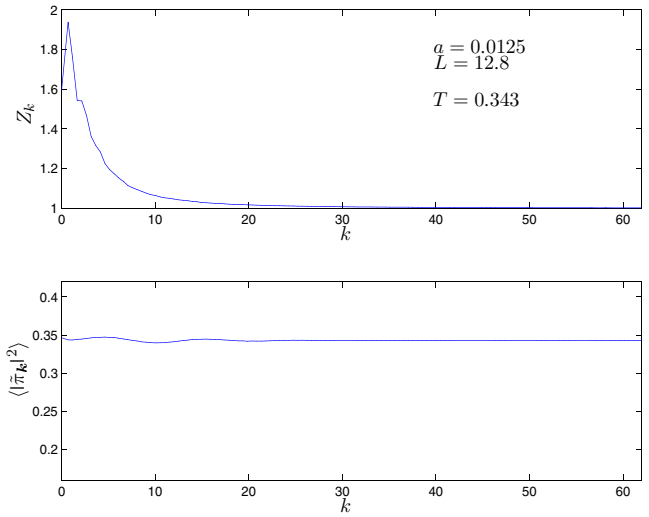

FIG. 3 (color online). Z_k vs the radial wave number (in the upper plot) and the power spectrum $\langle|\tilde{\pi}_{\boldsymbol{k}}|^2\rangle$ (lower plot), which is indeed almost flat and equal to the temperature T.

IV. DYNAMICS OF THERMALIZATION

We present here the exact evolution of the lattice ϕ^4 theory defined in Sec. II C and the development of the ultraviolet cascade. We considered three system sizes, $L = 6.4$, 12.8, and 25.6 and several lattice spacings, $a = 0.1$, 0.064, 0.05, 0.025, 0.0125, and 0.006 25. The largest system contains 1024^3 lattice sites. We worked with the largest volume 25.6^2 only for $a = 0.05$ and $E/V = 89.5$, verifying that the change from $L = 12.8$ to $L = 25.6$ does not change any observable in a significant way. Therefore $L = 12.8$ has been our preferred choice.

A. Initial conditions

We used a large variety of initial conditions in our calculations. In these studies the initial power is concentrated in the infrared; that is, $|\tilde{\phi}_{\boldsymbol{k}}|^2(0)$ and $|\tilde{\pi}_{\boldsymbol{k}}|^2(0)$ are significant only for wave numbers well below the cutoff $\Lambda = \pi/2a$. In particular, we considered superpositions of infrared plane waves, when the initial fields have the form

$$\begin{aligned}\phi(\boldsymbol{x},0) &= \phi_0 + A\sum_{i=1}^{K} c_i \cos(\boldsymbol{k}_i\cdot\boldsymbol{x} + 2\pi\gamma_i),\\ \pi(\boldsymbol{x},0) &= B\sum_{i=1}^{K} d_i \cos(\boldsymbol{k}_i\cdot\boldsymbol{x} + 2\pi\delta_i)\end{aligned} \tag{4.1}$$

as well as superpositions of localized wave packets of the form

$$\begin{aligned}\phi(\boldsymbol{x},0) &= \phi_0 + A\sum_i c_i w(\boldsymbol{x}-\boldsymbol{x}_i),\\ \pi(\boldsymbol{x},0) &= B\sum_i d_i w(\boldsymbol{x}-\boldsymbol{x}_i'),\end{aligned} \tag{4.2}$$

where

$$w(\boldsymbol{x}) = \sum_{\boldsymbol{n}\in\mathbb{Z}^3} w_0(k_{\max}[\boldsymbol{x} - L\boldsymbol{n}])$$

and $w_0(\boldsymbol{x})$ is either the Gaussian, $w_0(\boldsymbol{x}) = e^{-\boldsymbol{x}^2}$, or the Lorentzian, $w_0(\boldsymbol{x}) = (1+\boldsymbol{x}^2)^{-1}$. The sum over $\boldsymbol{n}$ in the last equation is needed by PBC, but in practice, with our choice $L \sim 10$, only a few terms in the sum are needed. These fields have support throughout Fourier space, but peaked as Gaussians or simple exponentials at low wave numbers $k \lesssim k_{\max}$.

In Eqs. (4.1) and (4.2), ϕ_0 is a uniform background, or homogeneous condensate, while the wave vectors $\boldsymbol{k}_i = 2\pi\boldsymbol{n}_i/L$ in Eq. (4.1) have nonzero modulus $|\boldsymbol{k}| \le k_{\max} \lesssim 30\pi/L = 15\pi/(Na) \ll \pi/(2a)$. The number K in Eq. (4.1) is chosen within the range 10–100, proportional to $k_{\max}$, and the specific $\boldsymbol{k}_i$ in Eq. (4.1) or the $\boldsymbol{x}_i$ and $\boldsymbol{x}_i$ in Eq. (4.2) are chosen at random. The phases γ_i, δ_i in Eq. (4.1) and the relative amplitudes c_i, d_i in both cases are chosen at random in the interval $[0, 1]$. Finally, for any given realization of these random numbers, the background ϕ_0 and the overall amplitudes A and B are constrained in such a way that the energy density E/V takes a given, predefined value. Typically, we further restricted the remaining freedom by choosing either $B = 0$ or $B = A$, so that the ''macroscopic'' part of the initial state is entirely characterized by the values of E/V, of the condensate ϕ_0, and of $k_{\max}$. In principle, one should then regard the randomly chosen numbers as ''microscopic,'' or fine-grained properties providing the initial entropy; one should then average all measured observables over these random choices, as described in Sec. II D, to reduce the fluctuations in the measures. Actually, we performed such an average (over 20 to 40 initial conditions) only rarely, since fluctuations were kept under control already by the 3D space average, by the sliding time average, and/or by the average over discrete directions of Appendix A.

It should be noticed that all our initial configurations have vanishing total momentum $\int d^3x\,\pi(\boldsymbol{x})\nabla\phi(\boldsymbol{x})$, which is a conserved quantity for PBC.

B. Time evolution of local observables

Here we show the time evolution of the basic local observables of Eq. (2.16) averaged in space and time according to Sec. II D. As mentioned above, we considered many different initial conditions, with several values of the energy density ranging from $E/V = 0.1$ up to $E/V = 5000$.

Figures 4–7 display the local observables $\overline{\pi^2}(t)$, $\overline{(\nabla\phi)^2}(t)$, $\overline{\phi^2}(t)$, and $\overline{\phi_+^4}(t)$ as functions of time for different values of the relevant parameters. When an initial zero-mode condensate is present [ϕ_0 in Eqs. (4.1) and (4.2)], we quantify its weight with the ratio E_0/E between the energy built solely from the zero mode and the total energy.

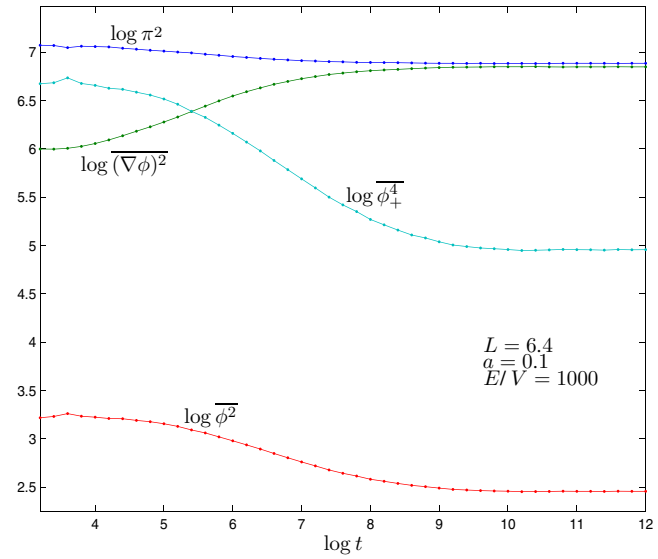

FIG. 4 (color online). Log-log plot of the time evolution of local observables with sliding time average. Initial conditions are localized wave packets of Lorentzian shape without any zero-mode condensate. No average is performed over initial packet amplitudes or positions.

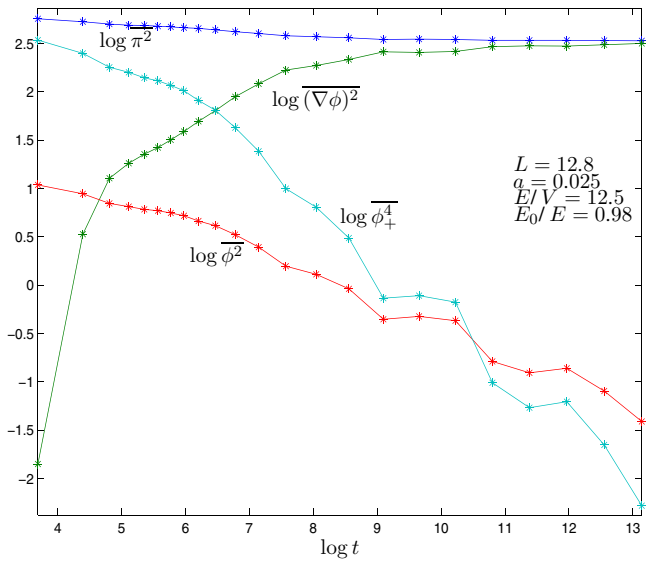

FIG. 6 (color online). Log-log plot of the time evolution of local observables. The time averaging interval is $\tau = 40$ and the initial conditions are plane waves with a large zero-mode condensate. No average is performed over initial amplitudes or phases.

These plots clearly reveal the main qualitative feature of the thermalization process in $3 + 1$ dimensions. Initially $\overline{(\nabla\phi)^2}(t)$ is small reflecting the fact that the initial conditions determine a power spectrum localized at wave vectors with $k \ll 1/a$. The mode mixing entailed by the interaction is transferring power to larger wave vectors, thus effectively transferring energy from the interaction and π^2 terms, which decrease, to the spatial gradient term which increases. As is clear from these figures, $\overline{\pi^2}(t)$ and $\overline{(\nabla\phi)^2}(t)$ tend to a limit for late time. $\overline{\phi^2}(t)$ and $\overline{\phi^4_+}(t)$ show a clear limiting behavior only for E/V large enough.

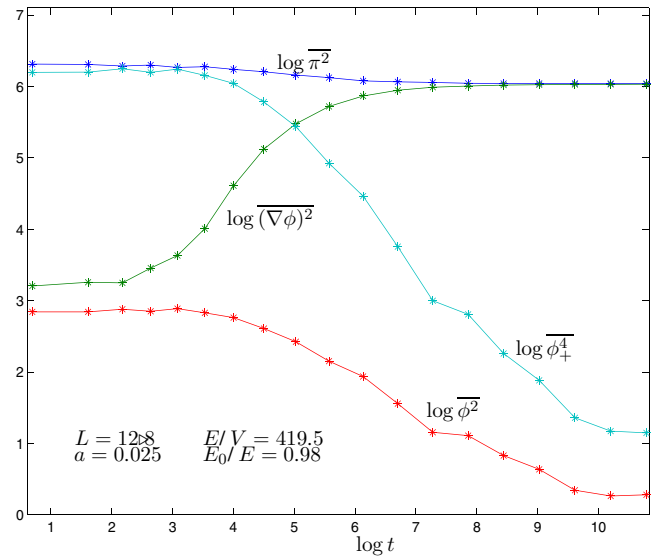

FIG. 5 (color online). Log-log plot of the time evolution of local observables. The time averaging interval is quite small, $\tau = 2$, and the initial conditions are plane waves with a large zero-mode condensate. No average is performed over initial amplitudes or phases.

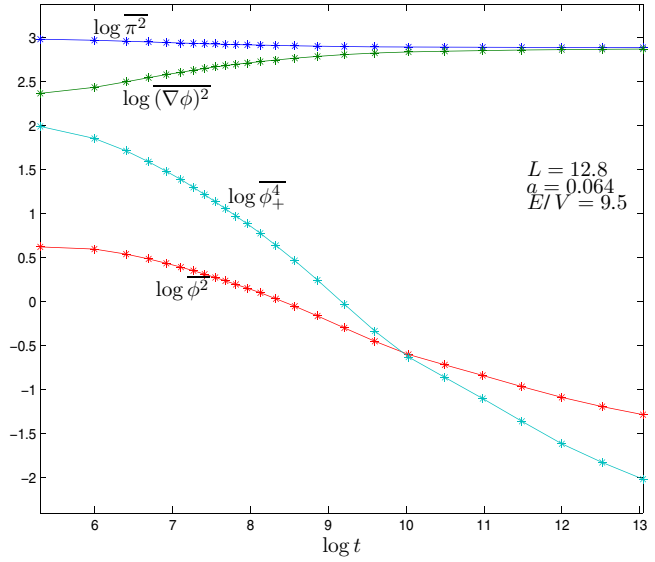

FIG. 7 (color online). Log-log plot of the time evolution of local observables. Initial conditions are plane waves without a zero-mode condensate. The time averaging interval is $\tau = 200$ and an extra average is performed over 40 random choices of initial amplitudes and phases. This explains why the curves in this picture are smoother than those in Figs. 5 and 6.

The steady growth of $\overline{(\nabla\phi)^2}(t)$ at the expense of the interaction term $\overline{\phi_+^4}(t)$, the kinetic energy $\overline{\pi^2}(t)$, and the mass term $\overline{\phi^2}(t)$ shows that the basic mechanism leading towards thermalization is a rather uniform flow of energy towards larger k modes, namely, the ultraviolet cascade. We can associate a time scale t_0 to the onset of this ultraviolet cascade by looking at the point when $\overline{(\nabla\phi)^2}(t)$ overtakes $\overline{\phi_+^4}(t)$, if such a point exists. For E/V too small, implying small field amplitudes and very small initial $\phi_+^4(0)$, $\overline{(\nabla\phi)^2}(t)$ might be larger than $\overline{\phi_+^4}(t)$ from the beginning. In this case we can take the point where the rise of $\overline{(\nabla\phi)^2}(t)$ is the steepest. From Figs. 4–7, as well as from the rest of our data, we see that t_0 does depend on E/V and on the condensate, but stays within the range $100 \lesssim t_0 \lesssim 400$ for E/V in the range from 10 to 5000, with t_0 decreasing as E/V increases at a fixed value of the condensate.

We are interested in somehow large energy densities E/V which are the relevant regime both for the early universe and the ultrarelativistic heavy ion collisions. However, it is physically interesting to also study the low energy density regime. We find that thermalization happens for small values of E/V. No threshold to a nonergodic behavior was found. However, the thermalization dynamics slows down dramatically when E/V is reduced well below a value ~ 10 and t_0 grows substantially. We depict in Fig. 8 $\overline{(\nabla\phi)^2}(t)$, $\overline{\dot{\phi}^2}(t)$, $\overline{\phi^2}(t)$, and $\overline{\phi_+^4}(t)$ for $E/V = 0.1$, $a = 0.1$, and $L = 6.4$. We see that the ultraviolet cascade only starts in this case for much later times $\ln t \simeq 11$, $t \simeq 50\,000$.

Figure 9 displays $\log|\overline{\phi}(t)|$ as a function of the logarithm of time for $E/V = 1000$, 10, and $E/V = 0.1$ for $L = 6.4$ and $a = 0.1$, respectively. We see that the relaxation of ϕ towards its thermal equilibrium value ($\phi = 0$) is different from the other physical quantities previously discussed. This is due to the fact that the vanishing of $\overline{\phi}$ is connected to a symmetry of the model. We find that $\overline{\phi}(t)$ relaxes as $\sim 1/t$ for $\ln t > \ln t_0 \simeq 6$, $t > t_0 \simeq 500$ in the universal stage. This can be seen from Fig. 9.

We plot in Fig. 10 $\langle\phi_+^4\rangle$ vs $\langle\phi^2\rangle$ in thermal equilibrium (obtained from Monte Carlo simulations) as well as $\overline{\phi_+^4}(t)$ vs $\overline{\phi^2}(t)$ from time averages. We see that the curve obtained from the lattice Monte Carlo calculations is in agreement with the ones from time averages. Since both $\overline{\phi_+^4}(t)$ and $\overline{\phi^2}(t)$ vary with time, the agreement with the thermal curve implies that, at least for these observables, we are in a situation of effective thermalization with a time depending temperature. As in Ref. [9] the effective temperature decreases with time. The small disagreement (less than 10%) between the thermal equilibrium curve (from Monte Carlo simulations) and the time averages in Fig. 10 comes from the low k modes contribution. As will be discussed below, infrared modes are much slower to thermalize than the modes with $k^2 > \overline{\phi^2}(t)$. Actually, the disagreement decreases with increasing time [decreasing $\overline{\phi_+^4}(t)$ and $\overline{\phi^2}(t)$] showing that the IR modes are getting thermalized equilibrating with the modes with $k^2 > \overline{\phi^2}(t)$.

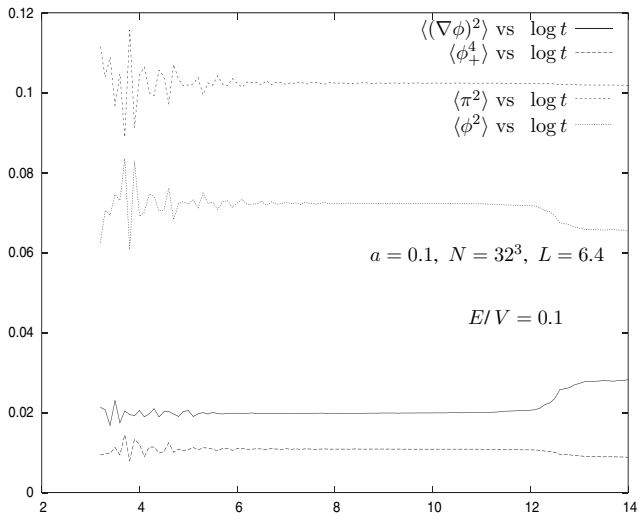

FIG. 8. Log-log plot of the time evolution of local observables with sliding time average and very small energy density. Initial conditions are of the same type as in Fig. 4. No average is performed over initial packet amplitudes or positions. Time averaging is performed here as by Eqs. (2.17) and (2.18).

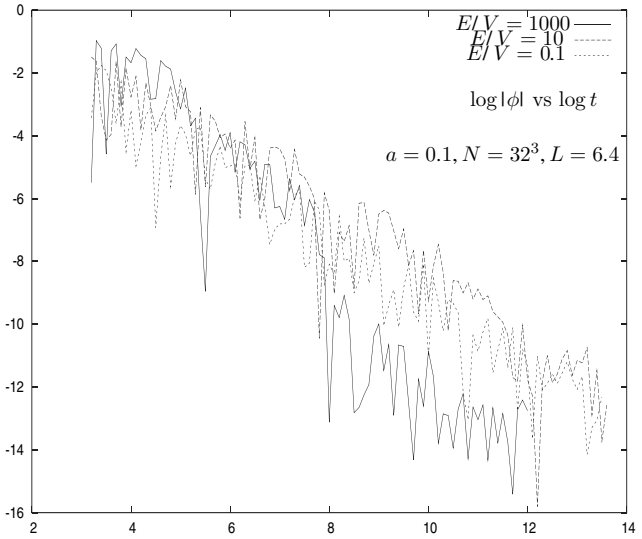

FIG. 9. $\log|\overline{\phi}(t)|$ as a function of the logarithm of the time t for $E/V = 1000$ and $E/V = 10$ with $L = 6.4$ and $a = 0.1$. No average is performed over initial packet amplitudes or positions. Time averaging is performed here as by Eqs. (2.17) and (2.18).

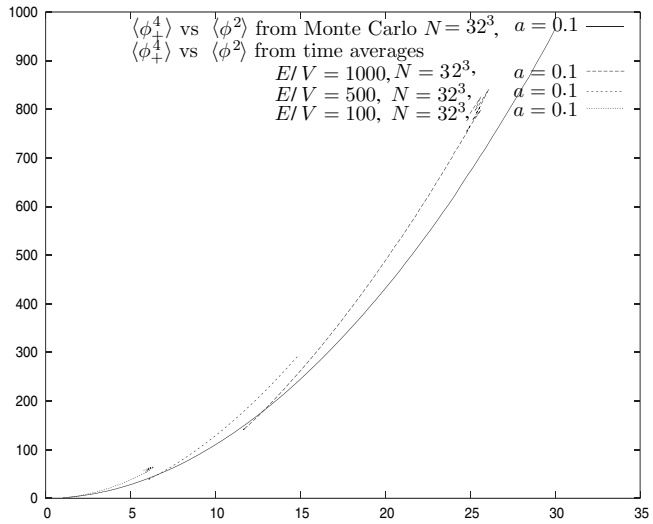

FIG. 10. $\langle\phi_+^4\rangle$ vs $\langle\phi^2\rangle$ in thermal equilibrium (obtained from Monte Carlo simulations) and $\overline{\phi_+^4}(t)$ vs $\overline{\phi^2}(t)$ from time averages. Both $\overline{\phi_+^4}(t)$ and $\overline{\phi^2}(t)$ decrease for increasing time.

C. Virialization and equation of state

We depict in Fig. 11 the quantity

$$\Delta(t) \equiv \frac{\langle\dot\phi^2\rangle(t) - \langle(\nabla\phi)^2\rangle(t) - \langle\phi^2\rangle(t) - \langle\phi_+^4\rangle(t)}{\langle\dot\phi^2\rangle(t)}. \quad (4.3)$$

This quantity vanishes when the virial theorem is fulfilled [see Eq. (3.6)]. It turns out to be negative for finite times and nonzero a. We see from Fig. 11 that $|\Delta(t)|$ starts to decrease at times earlier than t_0. Therefore, the model starts to virialize before it starts to thermalize. $|\Delta(t)|$ keeps decreasing with time and tends to a nonzero value which is of the order $\mathcal{O}(a^2)$ for $t\to\infty$. This is to be expected since Eq. (3.6) holds only in the continuum limit and receives corrections in the lattice $\mathcal{O}(a^2)$ as shown in Eq. (2.13).

We computed the pressure as a function of time from Eq. (3.10) as

$$\overline{p} = \tfrac{1}{2}[\overline{\dot\phi^2} - \tfrac{1}{3}\overline{(\nabla\phi)^2} - \overline{\phi^2} - \tfrac{1}{2}\overline{\phi_+^4}].$$

Notice that we are not using the virial theorem.

We depict in Fig. 12 $\overline{p}/\rho$ as a function of time. We see that

$$\frac{\overline{p}}{\rho} \lesssim \frac{1}{3}, \qquad t\to\infty,$$

for the whole range of ρ considered. This inequality is in agreement with Eq. (3.11). That is, Fig. 12 shows that the equation of state approaches approximately the radiation-dominated equation of state unless ρ is too small.

Notice from Figs. 4–7 and 12 that the approach to the radiation-dominated equation of state parallels the decrease of $\overline{\phi_+^4}$ since both are governed by the UV cascade.

We see that the virial as well as the equation of state reaches stationary values despite the fact that thermalization is not achieved. As already noticed in Ref. [8] the equation of state follows by taking a time average over the period for the cnoidal solution. Moreover, as we show in Appendix D, the virial theorem is exactly fulfilled by the cnoidal solution averaging over one period. This type of phenomena has been recently highlighted in Ref. [26].

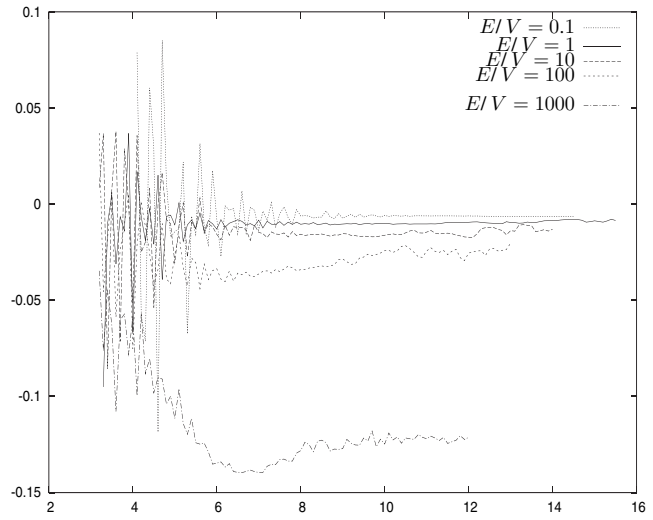

FIG. 11. The normalized left-hand side of the virial theorem $\Delta(t)$ vs the logarithm of the time t for $E/V=\rho=1$, 10, 100, and 1000 for $a=0.1$ and $L=6.4$ [see Eq. (4.3)]. No average is performed over initial packet amplitudes or positions. Time averaging is performed here as by Eqs. (2.17) and (2.18).

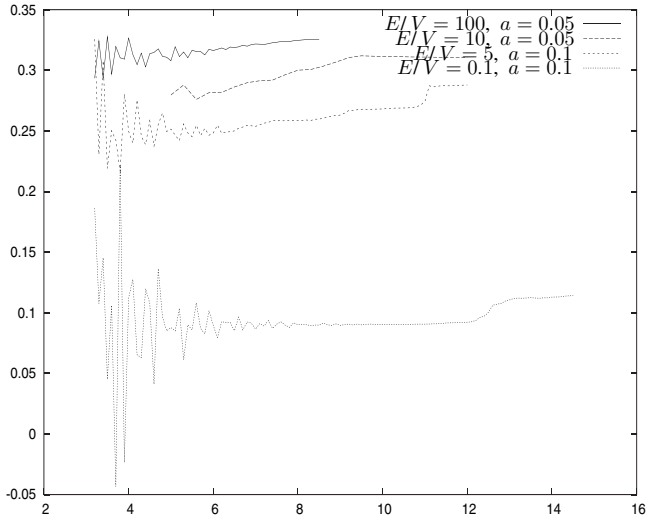

FIG. 12. The equation of state $\overline{p}/\rho$ vs the logarithm of the time t for $\rho=100$ and 10 with $a=0.05$ and for $\rho=5$ and 0.1 with $a=0.1$. We have in all four cases $L=6.4$. No average is performed over initial packet amplitudes or positions. Time averaging is performed here as by Eqs. (2.17) and (2.18).

D. Evolution of power spectra and UV cascade

We now turn our attention to the study of correlation functions.

According to the Fourier transform relationship Eq. (2.21) between the power spectrum $\overline{|\tilde{\phi}_k|^2}(t)$ and the equal-time correlation function $\overline{\phi\phi}(x, t)$, there are two approaches to the numerical evolution of such quantities (we specialize now on π but the discussion applies equally well to ϕ). We extract the field $\pi(\boldsymbol{x}, t)$ from the lattice fields $F(\boldsymbol{n}, s)$ and $G(\boldsymbol{n}, s)$ [see the first line in Eq. (2.8) and Eq. (2.14)], Fourier transform it to $\tilde{\pi}_{\boldsymbol{k}}(t)$, and then perform all needed averages on $|\tilde{\pi}_{\boldsymbol{k}}(t)|^2$. Or we directly compute averages of the correlations of $F(\boldsymbol{n}, s)$ and $G(\boldsymbol{n}, s)$ and extract from them the correlations $\overline{\pi\pi}(\boldsymbol{x}, t)$. We found that both methods yield the same results.

Moreover, when using the approach with growing time averages as in Eq. (2.18) with a unique initial condition, one realizes that the simply time-averaged correlation

$$\frac{1}{\tau}\int_{t-\tau}^{t} dt' \pi(\boldsymbol{x}, t')\pi(\boldsymbol{x}', t') \tag{4.4}$$

very soon (in the logarithm of time) becomes translation invariant, that is a function only on the distance $|\boldsymbol{x} - \boldsymbol{x}'|$, making the time consuming space average unnecessary.

Figures 13 and 14 show the average power $\overline{|\tilde{\pi}_k|^2}(t)$, multiplied by the spherical measure $4\pi k^2$, for five values of the lattice spacing and one given choice of all other parameters. The region where the power is significant is spreading towards the UV cutoff.

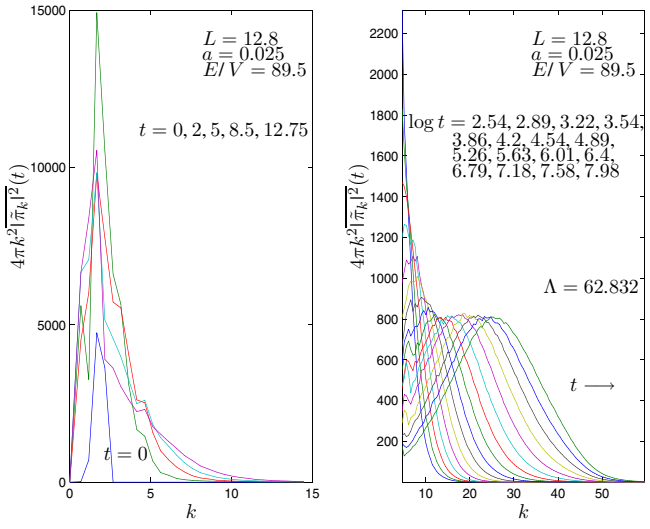

FIG. 13 (color online). The power $4\pi k^2\overline{|\tilde{\pi}_k|^2}(t)$ vs $k = |\boldsymbol{k}|$ at 20 different times ranging, in an approximately exponential way, from $t = 0$ to $t = 12.75$ (left panel) and from $t = 12.75$ to $t = 2948$ (right panel). The time averaging interval is $\tau = 2$ and the initial conditions are infrared random plane waves, as apparent from the IR peaks at early times. The front of the UV cascade arrives close to the cutoff Λ for the latest times.

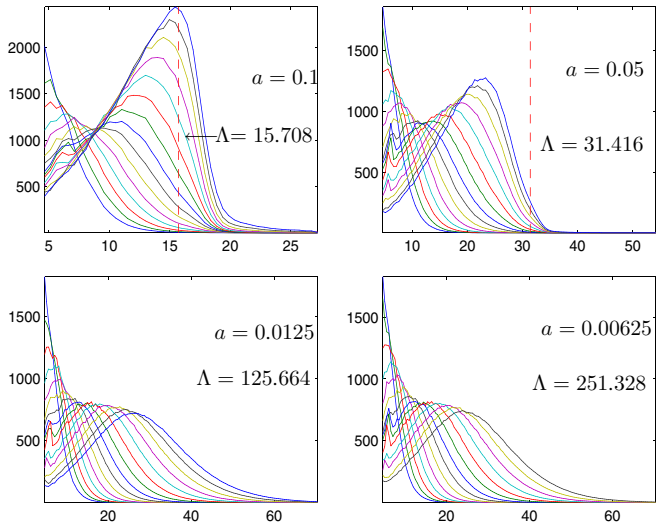

FIG. 14 (color online). The power $4\pi k^2\overline{|\tilde{\pi}_k|^2}(t)$ vs k as in the right of Fig. 13 but at values of the UV cutoff Λ scaled by $1/4$, $1/2$, 2, and 4. When $\Lambda = 251.328$ the last time $t = 2978$ is missing. The cascades shown in the lower panels are cutoff independent since they are evolving well below the cutoff Λ.

The chosen initial conditions Eqs. (4.1) and (4.2) are such that the power is concentrated in long wavelength modes with k well below the ultraviolet cutoff $\Lambda = \pi/(2a)$. Therefore, $\overline{|\tilde{\pi}_k|^2}(0)$ is concentrated on small k. During the time evolution the nonlinearity gradually transfers energy off to higher k modes leading to the ultraviolet cascade as discussed above.

It is important to observe the effects of the finite UV cutoff Λ. At the given value $E/V = 89.5$ of the energy density, when $\Lambda = 62.832$ (Fig. 13), which corresponds to a lattice with 256^3 sites, the shape as a function of k and the time evolution of the power spectrum are still markedly distorted by the presence of the cutoff, although much less than for the smaller values $\Lambda = 15.708$ and $\Lambda = 31.416$ (Fig. 14). Only when doubling the cutoff from 125.664 to 251.328 (corresponding respectively to 512^3 and 1024^3 lattices) the effect of the cutoff in $\overline{|\tilde{\pi}_k|^2}(t)$ does not appear significant.

That is, the cascades shown in the lower panels of Fig. 14 are cutoff independent since they are evolving well below the cutoff Λ.

Plots analogous to Figs. 13 and 14 can be drawn for the field power $k^2\overline{|\tilde{\phi}_k|^2}(t)$. However, since unlike $k^2\overline{|\tilde{\pi}_k|^2}(t)$, $k^2\overline{|\tilde{\phi}_k|^2}(t)$ never grows with k [at thermal equilibrium and in the continuum $\overline{|\tilde{\phi}_k|^2}(t)$ goes like k^{-2}, see Sec. III B], the UV cascade for $k^2\overline{|\tilde{\phi}_k|^2}(t)$ is not as evident as for $k^2\overline{|\tilde{\pi}_k|^2}(t)$. The time evolution of both powers can be better appreciated in Figs. 15 and 16. One can see a rather complicated behavior in the strongly interacting infrared, while the rest of the modes exhibit a rather orderly evolution which indicates a weakly interacting dynamics.

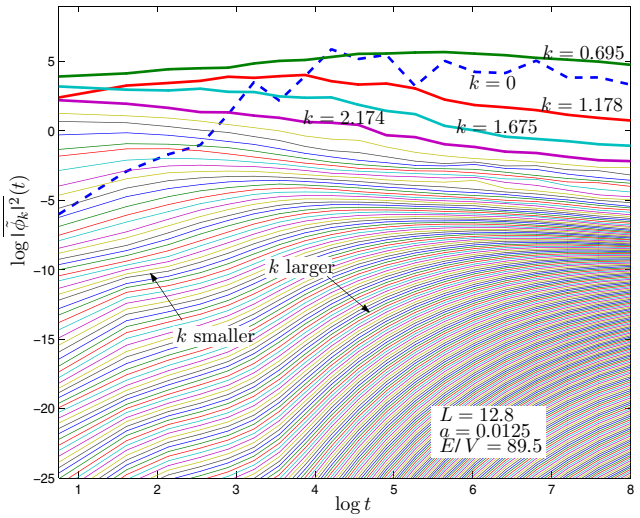

FIG. 15 (color online). Log-log plot of $\overline{|\tilde{\phi}_k|^2}(t)$ vs time. Initial conditions are as in Fig. 13. The four thicker lines correspond to the modes initially filled (after averaging over directions). The zero-mode (dashed line) was not filled at $t = 0$. Notice the peculiar behavior of the lowest k modes compared with the rest of the k modes.

One sees from Figs. 15 and 16 that modes with low k decrease in amplitude with time except for $k = 0$ and the first two nonzero modes. Modes with larger k grow in amplitude monotonically with time showing the existence of the smooth UV cascade. Since total energy is conserved the larger k modes grow in amplitude at the expense of the lower k modes. Notice that only a restricted number of low k modes have a significant initial amplitude. They feed the growth of a large number of modes with larger k which

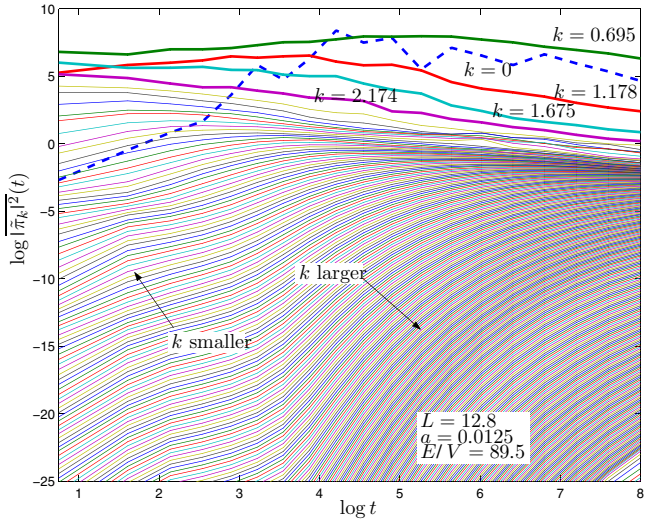

FIG. 16 (color online). As in Fig. 15, but for $\overline{|\tilde{\pi}_k|^2}(t)$ vs time. Notice the peculiar behavior of the lowest k modes compared with the rest of the k modes.

start with very small initial amplitudes. Later, for $t \gtrsim t_0$ all IR modes decrease with time.

As said before, the $k = 0$ mode and the first two nonzero modes in Figs. 15 and 16 behave differently to the rest of the modes. They start by growing with time and they stay larger than all the other modes for a while. Actually, as we shall see below in Sec. IV I, the modes with $0 \leq k \lesssim \sqrt{\overline{\phi^2}}(t)$ behave differently to the rest keeping a significant coupling among them while modes with $k \gtrsim \sqrt{\overline{\phi^2}}(t)$ exhibit weak nonlinearities for late times in the lattice model. More precisely, these latter modes obey the Hartree approximation and exhibit effective equilibration much earlier than the infrared modes.

A single parameter that efficiently measures the UV cascade for $\overline{|\tilde{\pi}_k|^2}(t)$ is the average wave number $\overline{k}(t)$, defined [in continuum notation and recalling the sum rules Eq. (2.20)] as

$$\frac{1}{\overline{\pi^2}(t)} \int_{-\Lambda}^{\Lambda} \frac{d^3k}{(2\pi)^3} |k| \overline{|\tilde{\pi}_k|^2}(t). \tag{4.5}$$

However, it will be more appropriate to exclude from the integration in Eq. (4.5) the infrared modes. More precisely, since for the evolution time considered, a large portion of energy lingers on the IR modes filled at $t = 0$ (see Fig. 16), one should restrict the averaging over the modes not filled at $t = 0$ and define more properly, after averaging over discrete directions,

$$\overline{k}(t) = \frac{1}{P} \int_{k_0}^{\Lambda} \frac{k^2 dk}{2\pi^2} k \overline{|\tilde{\pi}_k|^2}(t), \qquad P = \int_{k_0}^{\Lambda} \frac{k^2 dk}{2\pi^2} \overline{|\tilde{\pi}_k|^2}(t), \tag{4.6}$$

where k_0 is the smallest unfilled radial wave number larger than all wave numbers of the modes filled at $t = 0$. This procedure applies directly when the initial conditions are a superposition of IR plane waves. In the case of superposition of localized wave packets, k_0 may be defined as the value of k at which $|\tilde{\pi}_k|^2(0)$ drops below some fixed small value.

We plot $\overline{k}(t)$ in Fig. 17 for the same context of Figs. 13 and 14. The cutoff effects at larger values of a and the saturation in the continuum limit $a \to 0$ are quite evident. Still, in spite of the fact that the UV cascade has time to fully develop, as evident from Figs. 13 and 14, Fig. 17 shows that the growth of $\overline{k}(t)$ with time is not a simple power, not even for the latest times considered. However,

$$\overline{k}(t) \sim k_0 t^{1/3} \tag{4.7}$$

provides a rough estimate.

Let us now turn our attention to the behavior in k of $\overline{|\tilde{\pi}_k|^2}(t)$ during the UV cascade. From all our data, it is clear that $\overline{|\tilde{\pi}_k|^2}(t)$ dies exponentially fast for $k > \overline{k}(t)$ as long as $\overline{k}(t) \ll \Lambda$ (see Fig. 18 as an example). This exponential behavior is clearly time dependent. For k not too

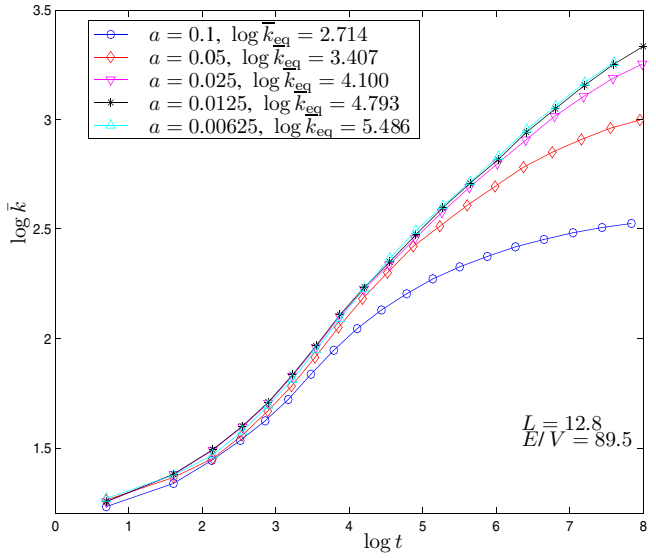

FIG. 17 (color online). Log-log plot of the time evolution of average wave number $\overline{k}(t)$, for five values of the lattice spacing $2a$, with initial conditions as in Figs. 13 and 14.

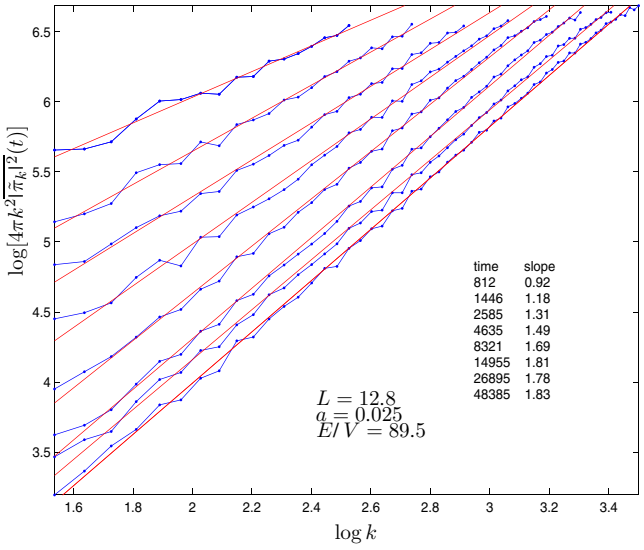

FIG. 19 (color online). $\log[4\pi k^2 \overline{|\tilde{\pi}_k|^2}(t)]$ vs $\log k$ in a fixed wave number window for several values of time. All relevant parameters are at the indicated values.

small nor too close to $\overline{k}(t)$, $\overline{|\tilde{\pi}_k|^2}(t)$ exhibits a decreasing powerlike behavior, as can be seen for instance in Fig. 19, where the log-log plot of $4\pi k^2 \overline{|\tilde{\pi}_k|^2}(t)$ vs k is shown. That is, $\overline{|\tilde{\pi}_k|^2}(t) \sim k^{-\alpha}$ at different times, where the values of $-\alpha$ are obtained subtracting 2 from the numbers indicated in Fig. 19. α decreases monotonically from 1.12 at $t = 812$ to 0.17 at $t = 48\,385$, when the forefront of the cascade is reaching the cutoff Λ.

In Figs. 20 and 21 we give some graphic examples of the UV cascade in the presence of an initial zero-mode condensate [ϕ_0 in Eqs. (4.1) and (4.2)]. We notice the evidence for the parametric resonance, whose location in k space well agrees with the analytic prediction from the solution of the Lamé equation for the linearized model [see Eq. (B7)]. It is quite evident however, that such parametric resonance plays practically no role in the UV cascade, as already noticed in Ref. [21]. We also stress once more the importance of UV cutoff effects when a is doubled from

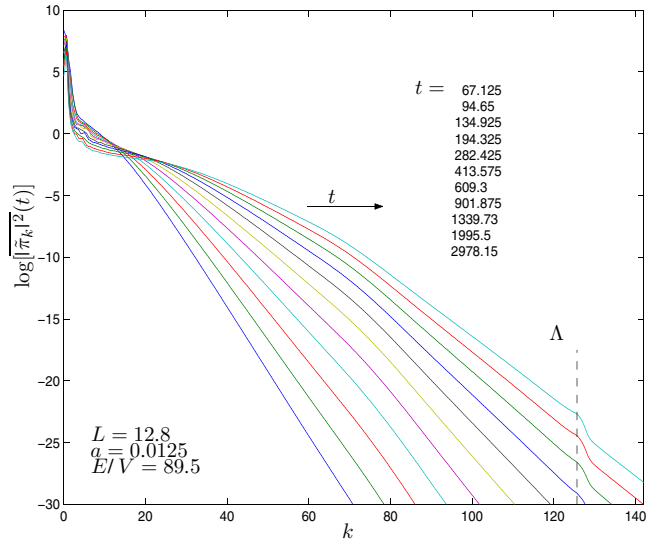

FIG. 18 (color online). $\log[\overline{|\tilde{\pi}_k|^2}(t)]$ vs k for several values of time. All relevant parameters are at the indicated values. Initial conditions were random plane waves. $\overline{|\tilde{\pi}_k|^2}(t)$ starts decreasing with k as $\sim k^{-\alpha}$ and later it dies exponentially for $\Lambda > k > \overline{k}(t)$.

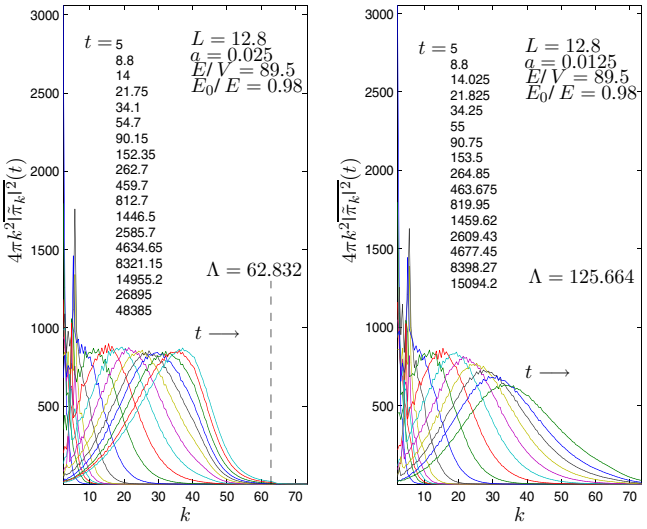

FIG. 20 (color online). The power $4\pi k^2 \overline{|\tilde{\pi}_k|^2}(t)$ vs $k = |\boldsymbol{k}|$ at several times, $E/V = 89.5$ and two lattice spacings. The initial conditions are infrared random plane waves with a zero-mode condensate dominating the energy. Notice the peaks due to parametric resonance.

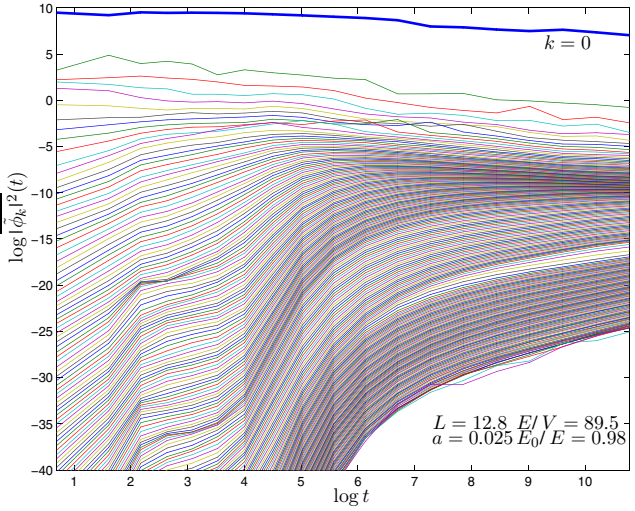

FIG. 21 (color online). Log-log plot of $\overline{|\tilde{\phi}_k|^2}(t)$ vs time. Initial conditions are as in Fig. 20. Only the zero-mode (thick line) was macroscopically filled at $t = 0$.

$a = 0.0125$ to $a = 0.025$ (corresponding to a reduction of the lattice from 512^3 to 256^3 sites). This is particularly relevant since the zero mode (and a few lower k modes) remains quite large for all times considered (see Fig. 21): according to the scenario of Ref. [21], the regime should then remain that of driven turbulence until the lattice effect becomes dominant; thus, for the energy density of Figs. 20 and 21, no cutoff-independent regime of free turbulence is observable in our evolution when $a = 0.025$ and $L = 12.8$. (Notice that our lattices reach a size 4^3 times larger than those in Ref. [21].)

It would indeed be very interesting to find this universal UV cascade in quantum theory for large occupation numbers and small couplings. Most of the works consider other regimes [10–12]. In Ref. [27] the small coupling regime in quantum theory is investigated including the leading $1/N$ corrections. However, thermalization is not reached in Ref. [27] since the times considered are not long enough. The classical evolution is compared with the quantum evolution to first order in $1/N$ for the ϕ^4 model in $3 + 1$ dimensions in Ref. [17]. It is stated there that the classical evolution is a good approximation to the quantum evolution for nonasymptotic times therefore supporting the relevance for quantum field theory of the classical dynamics studied here.

E. Thermalization of the power spectra

We present here the results of a long simulation yielding to a very good approximation thermalized powers $\overline{|\tilde{\pi}_k|^2}(t)$ and $\overline{|\tilde{\phi}_k|^2}(t)$, on a lattice cube C_N with $N = 100$, $a = 0.064$, and $L = 12.8$. The energy density is $E/V = 569.5$, still relatively small compared to $\Lambda^3 \simeq 14\,785$. The initial conditions are random plane waves as in Eq. (4.1), with the initial powers of ϕ and π exactly null for $k > 3.436$. The rather large time averaging interval $\tau = 200$ is still negligible compared to the length $t = 915\,494$ of the evolution. To further reduce fluctuations, in this case we also performed an average of over 32 different random initial mode amplitudes and phases.

In Fig. 22 we plot the basic one-point observables and the average wave number $\overline{k}(t)$ as a function of time. The system clearly reaches a time-independent stage for $\ln t \gtrsim 12.5$. In Fig. 23 we plot the power spectra $\overline{|\tilde{\pi}_k|^2}(t)$, times the spherical volume $4\pi k^2$, vs the wave number k at several times: the UV cascade up to the cutoff is evident. We plot in a log-log scale both $\overline{|\tilde{\pi}_k|^2}(t)$ and $\overline{|\tilde{\phi}_k|^2}(t)$ vs k in Fig. 24 and vs time in Fig. 25. Again, the system shows an evident limiting behavior: the large initial peaks in the IR modes have almost completely disappeared for $\log t \simeq 12.5$ and at the latest times $\log t \simeq 14$ the power spectrum $\overline{|\tilde{\pi}_k|^2}(t)$ is flat, except for fluctuations and a small remnant of the infrared peaks exactly at $k = 0$ (see top panel in Fig. 26). From the height of $\overline{|\tilde{\pi}_k|^2}(t)$ in the plateau we read the temperature $T = 1.2$, very close to $E/N^3 = 1.194\,32\cdots$. The difference is almost completely accounted for by the last value of $\overline{\phi_+^4} = 10.264\cdots$ [see Eq. (3.8)].

To ascertain the thermalization of $\overline{|\tilde{\phi}_k|^2}(t)$ is very convenient to consider the time-dependent analog $Z_{\boldsymbol{k}}(t)$ of the equilibrium $Z_{\boldsymbol{k}}$ [see Eq. (3.28)] replacing the equilibrium quantities by their time-dependent out-of-equilibrium counterparts; that is

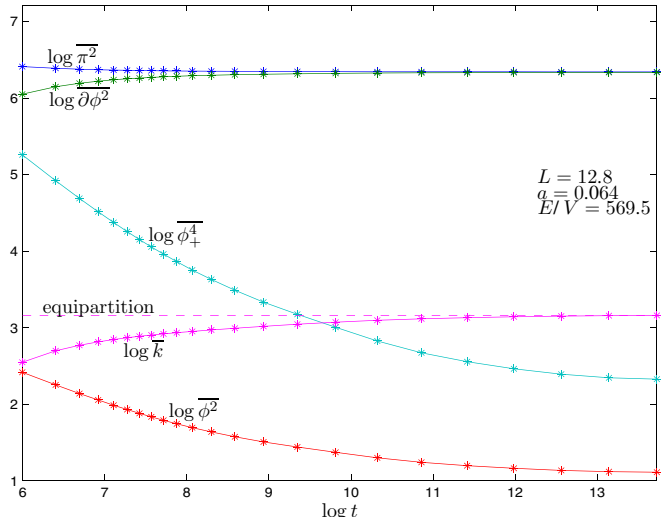

FIG. 22 (color online). Log-log plot of the time evolution of space-averaged local observables and of the average wave number. The time averaging interval is $\tau = 200$ and the initial conditions are infrared random plane waves. This plot is analogous to Fig. 5 but with the time evolution lasting for significantly later times.

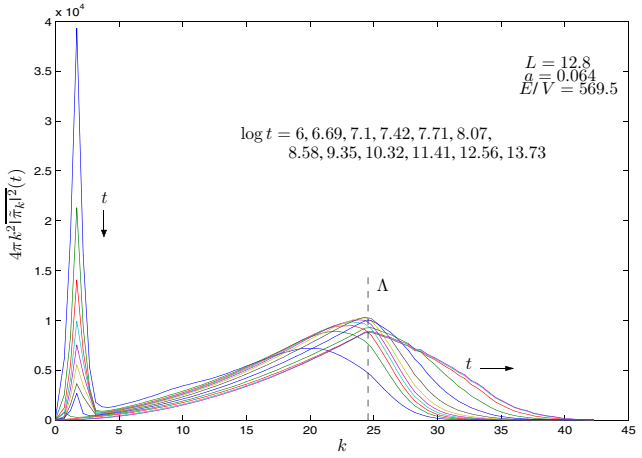

FIG. 23 (color online). $4\pi k^2\overline{|\tilde{\pi}_k|^2}(t)$ vs k at the times indicated. All parameters are as in Fig. 22.

$$Z_{\boldsymbol{k}} * t) \stackrel{\text{def}}{=} \frac{1 - [B(\overline{\phi^2}(t))C(\boldsymbol{k}a)]^2}{a^2\overline{|\tilde{\pi}_{\boldsymbol{k}}|^2}(t)}\overline{|\tilde{\phi}_{\boldsymbol{k}}|^2}(t). \tag{4.8}$$

In the bottom panel of Fig. 26 we plot the (average over discrete directions of) equilibrium Z_k and $Z_k(t)$ for several late times. It is evident that $Z_k(t)$ approaches its equilibrium value Z_k earlier and much more closely than $\overline{|\tilde{\pi}_k|^2}(t)$. In other words, when both $\overline{|\tilde{\pi}_k|^2}(t)$ and $\overline{|\tilde{\phi}_k|^2}(t)$ are still out of equilibrium over a wide range of low wave numbers, $Z_k(t)$ is practically already at equilibrium except for a very narrow range of very small wave numbers. One can see that this range is approximately given by $k^2 < \overline{\phi^2}(t)$. These infrared modes are the last to effectively thermalize. (Recall Figs. 15 and 16 and the discussion in Sec. IV D about the peculiar behavior of these low k modes.)

In conclusion, the field does thermalize completely in the lattice with a time scale of the order 10^6. For such times $\overline{|\tilde{\pi}_{\boldsymbol{k}}|^2}(t)$ is k independent as seen in Fig. 24. Contrary to the $1 + 1$ dimensional case [9], the infrared modes with $k^2 < \overline{\phi^2}(t)$ thermalize here the last.

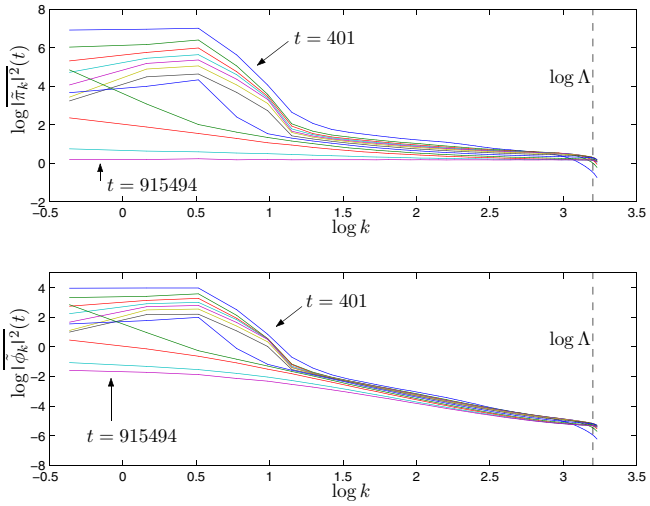

FIG. 24 (color online). Log-log plot of $\overline{|\tilde{\pi}_k|^2}(t)$ and $\overline{|\tilde{\phi}_k|^2}(t)$ vs k. Data points are explicitly indicated. All parameters are as in Fig. 22. Comparison with Fig. 22 shows that modes with $k^2 < \overline{\phi^2}(t)$ thermalize much slower than those with $k^2 > \overline{\phi^2}(t)$.

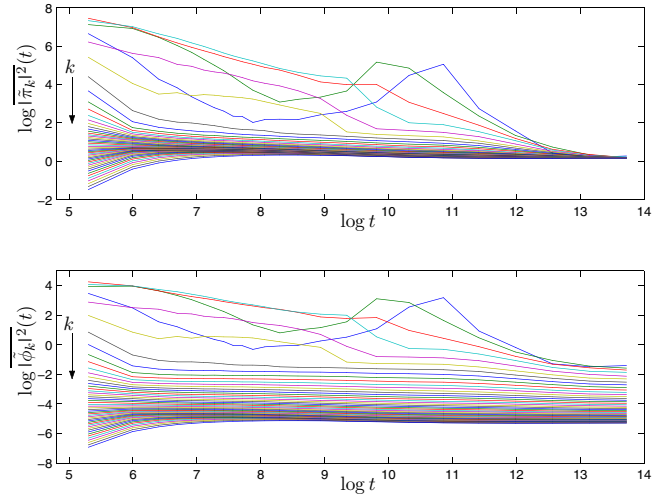

FIG. 25 (color online). Log-log plot $\overline{|\tilde{\pi}_k|^2}(t)$ and $\overline{|\tilde{\phi}_k|^2}(t)$ vs $\ln t$. Only modes up to $k \leq \Lambda$ are shown. All parameters are as in Fig. 22. We see that modes with $k^2 < \overline{\phi^2}(t)$ thermalize here the last. [Compare with Fig. 22 to see $\log\overline{\phi^2}(t)$.]

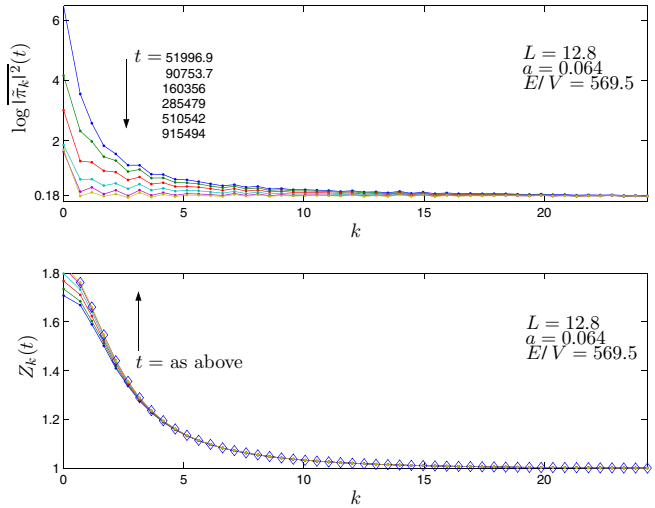

FIG. 26 (color online). Comparison of $\log\overline{|\tilde{\pi}_k|^2}(t)$ vs $Z_k(t)$. Diamonds in the bottom panel represent equilibrium values. All parameters are as in Fig. 22. We see that $Z_k(t)$ equilibrates much earlier than $\overline{|\tilde{\pi}_k|^2}(t)$.

F. Equilibration in the cascade

The effectiveness of the $Z_{\boldsymbol{k}}(t)$ in the study of the equilibration process for very late times suggests to use it also at earlier times, during the universal UV cascade. As a matter of fact, Eq. (4.8) is just the *definition* of $Z_{\boldsymbol{k}}(t)$ and is possible for any time, although it might very well turn out to yield a function of $\boldsymbol{k}$ quite different from its equilibrium counterpart $Z_{\boldsymbol{k}}$. What we find, however, is something very close to equilibrium already at times of order $t_0 \simeq 500$, which are those proper of the universal cascade. To have a cutoff-independent window wide enough, we consider here a lattice spacing $a = 0.0125$, much smaller than that of the previous section, and a smaller energy density $E/V = 89.5$. Notice that this would correspond to an equilibrium temperature of order $E/N = 0.001\,398\cdots$, almost negligible as compared to that of the previous section.

In Fig. 27, in the left column, we plot $Z_k(t)$, the direction averaged $Z_{\boldsymbol{k}}(t)$, for several times ranging from $t = 135$ to $t = 2978$ and for $0.695\cdots \le k \le 9.559\cdots$ in the top and $4.644\cdots \le k \le 28.218\cdots$ in the bottom. In the left column, we plot $Z_k(t)$ vs the scaled wave number $u = k/\sqrt{\overline{\phi^2}(t)}$. The good collapse in the bottom left panel shows that $Z_k(t)$ is an almost function only of u in the range $3.430\cdots \le u \le 20.843\cdots$. The collapse for $0.513 \le u \lesssim 2.5$ is definitely worse, in agreement with the slower equilibration of the infrared modes. Most remarkably, by direct comparison with Fig. 26, we observe that $Z_k(t)$ is very similar, qualitatively and quantitatively, to its equilibrium counterpart at a temperature roughly 1000 times larger than the temperature the system will eventually reach when $t \to \infty$. One could say that equilibration in the bulk of cascade has taken place with an effective temperature of order 1. The precise time dependence of this effective temperature as well as a check on its universality (that is to say unicity when the studied observables are changed) requires a much more elaborate analysis which is beyond the scope of the present work. Here we stress only that, as a function of u, $Z_k(t)$ resembles closely its equilibrium counterpart and, in particular, it decreases to unity rather fast as u grows, that is when $k^2 \gg \overline{\phi^2}(t)$.

G. Effective frequency and particle number

The motion of each Fourier mode $\tilde{\phi}_{\boldsymbol{k}}$ of the field is characterized by fast oscillations into an envelope which varies relatively slowly in time. In the linear approximation, the scale of fast oscillation is fixed by the frequency of the free massive dispersion relation, that is $\omega_k = k^2 + 1$ in the continuum. Of course on our staggered lattice one should consider the lattice dispersion relation, which differs from the continuum form by power corrections in $a^2\boldsymbol{k}^2$. In Appendix B we show that the exact free dispersion relation on our lattice reads

$$\cos(\omega_{\boldsymbol{k}} a) = \frac{1}{1 + \frac{1}{2}a^2} \prod_{j=1}^{3} \cos k_j a \tag{4.9}$$

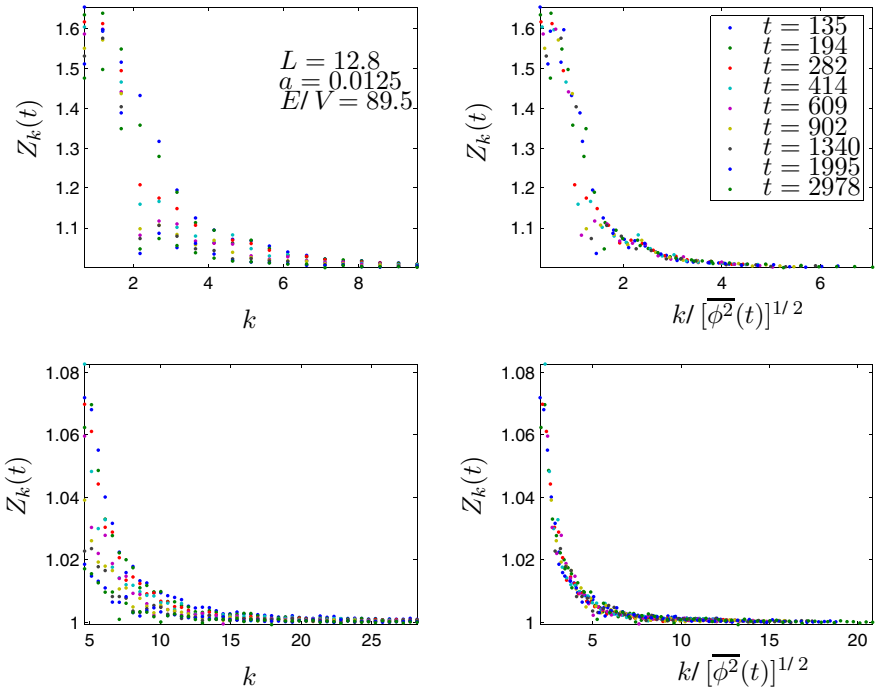

FIG. 27 (color online). Scaling properties of the $Z_k(t)$ for two low-lying ranges of the radial wave number k.

which correctly reproduces $k^2 + 1$ in the limit $a \to 0$ at fixed $\boldsymbol{k}$.

On the continuum the modes $\tilde{\phi}_{\boldsymbol{k}}$ obey the Fourier transform of the exact field equation (2.3), namely,

$$\frac{d^2}{dt^2}\tilde{\phi}_{\boldsymbol{k}} = -\omega_k \tilde{\phi}_{\boldsymbol{k}} - (\tilde{\phi}^3)_{\boldsymbol{k}}, \tag{4.10}$$

where $(\tilde{\phi}^3)_{\boldsymbol{k}}$ is the Fourier transform of $\phi^3(x)$.

Now to disentangle fast and slow motions one can use time averages over intervals large compared to the periods of the fast oscillations but small compared to the time scale of the slow motion. This is exactly what we did above, revealing the smooth UV cascade. To give a quantitative description of this scenario we can use the following simple argument. Consider the quantity

$$I_{\boldsymbol{k}} = \frac{d}{dt}(\mathrm{Re}\tilde{\phi}_{-\boldsymbol{k}}\tilde{\pi}_{\boldsymbol{k}}).$$

If the motion of each mode were strictly periodic, the time average over several periods of $I_{\boldsymbol{k}}$ would vanish. But this is also true if the fast and slow motions are indeed separable, at least after some coarse graining like averaging over discrete directions. Then we may proceed as in the standard derivation of the virial theorem and obtain, by use of the equation of motion (4.10),

$$\overline{|\tilde{\pi}_{\boldsymbol{k}}|^2} = \omega_k^2\overline{|\tilde{\phi}_{\boldsymbol{k}}|^2} + \mathrm{Re}[\overline{\tilde{\phi}_{-\boldsymbol{k}}(\tilde{\phi}^3)_{\boldsymbol{k}}}].$$

We may now define the effective frequency $\Omega_{\boldsymbol{k}}$ as

$$\Omega_{\boldsymbol{k}}^2 \equiv \frac{\overline{|\tilde{\pi}_{\boldsymbol{k}}|^2}}{\overline{|\tilde{\phi}_{\boldsymbol{k}}|^2}} = \omega_k^2 + \mathrm{Re}\left[\frac{\overline{\tilde{\phi}_{-\boldsymbol{k}}(\tilde{\phi}^3)_{\boldsymbol{k}}}}{\overline{|\tilde{\phi}_{\boldsymbol{k}}|^2}}\right], \tag{4.11}$$

where, with the exception of ω_k^2, everything depends on time, but only according to the slow motion.

Our aim here is to derive a quasiparticle description for the classical evolution. Quasiparticle pictures have been successfully derived in the context of the Hartree approximation both classically and quantum mechanically (see, for example, Refs. [7,8,18,19,28]).

On the staggered lattice there are purely kinematic modifications to Eq. (4.11), since the fields satisfy discrete recursion relations rather than differential equations. In Appendix B we derive the virial theorem for the free discrete dynamics on the staggered lattice. A comparison of Eq. (B6) with Eq. (4.11) suggests the following lattice relation for the effective frequency $\Omega_{\boldsymbol{k}}$:

$$\frac{\overline{|\tilde{\pi}_{\boldsymbol{k}}|^2}}{\overline{|\tilde{\phi}_{\boldsymbol{k}}|^2}} = \frac{1}{a^2}\left[1 - \left(1 - \frac{1}{4}a^4\right)\cos^2(\Omega_{\boldsymbol{k}} a)\right]. \tag{4.12}$$

After averaging over discrete directions, we obtain the following practical rule for calculating the lattice direction-independent effective frequency:

$$\left(1 - \frac{1}{4}a^4\right)\cos^2(\Omega_k a) \simeq 1 - a^2\frac{\overline{|\tilde{\pi}_k|^2}}{\overline{|\tilde{\phi}_k|^2}}. \tag{4.13}$$

Equation (4.13) suggests also a way to parametrize the equilibrium two-point function $\langle|\tilde{\phi}_{\boldsymbol{k}}|^2\rangle$ on the lattice in terms of an equilibrium effective frequency $\Omega_{\boldsymbol{k}}^{\mathrm{eq}}$: replacing $\overline{|\tilde{\pi}_k|^2}$ by its equilibrium counterpart $\langle|\tilde{\pi}_{\boldsymbol{k}}|^2\rangle = T$ and $\overline{|\tilde{\phi}_k|^2}$ by $\langle|\tilde{\phi}_{\boldsymbol{k}}|^2\rangle$ yields

$$\langle|\tilde{\phi}_{\boldsymbol{k}}|^2\rangle = \frac{a^2 T}{1 - (1 - \frac{1}{4}a^4)\cos^2(\Omega_{\boldsymbol{k}}^{\mathrm{eq}} a)}. \tag{4.14}$$

Going back to the continuum, we recall that the Hartree approximation for $\Omega_{\boldsymbol{k}}$ follows from the reduction of

$$(\tilde{\phi}^3)_{\boldsymbol{k}} = \frac{1}{V}\sum_{\boldsymbol{q}\boldsymbol{q}'}\tilde{\phi}_{\boldsymbol{q}}\tilde{\phi}_{\boldsymbol{q}'}\tilde{\phi}_{\boldsymbol{k}-\boldsymbol{q}-\boldsymbol{q}'}$$

to the sum of all terms proportional to $\tilde{\phi}_{\boldsymbol{k}}$, that is

$$(\tilde{\phi}^3)_{\boldsymbol{k}}^{\mathrm{H}} = \frac{3}{V}\sum_{\boldsymbol{q}}|\tilde{\phi}_{\boldsymbol{q}}|^2\tilde{\phi}_{\boldsymbol{k}} = \frac{3}{V}\tilde{\phi}_{\boldsymbol{k}}\int_V d^3x\phi^2(x).$$

Using Eq. (4.11) this yields the Hartree frequency,

$$(\Omega_{\boldsymbol{k}}^{\mathrm{H}})^2 = \omega_k^2 + 3\overline{\phi^2}(t). \tag{4.15}$$

It must be noticed that the same effective frequency follows by using the Whitham approach [29]. That is, considering a multiwave configuration as in Eq. (4.1), the first nonlinear correction to the frequency in the Whitham approach can be shown after some work to coincide with the Hartree formula Eq. (4.15).

Taking into account the definition of $Z_k(t)$ as defined by Eq. (4.8), we now have

$$Z_k(t) \equiv \frac{\overline{|\tilde{\phi}_k|^2}}{a^2\overline{|\tilde{\pi}_k|^2}}\left[1 - \left(1 - \frac{1}{4}a^4\right)\cos^2(a\Omega_k^{\mathrm{H}})\right] = \frac{(\Omega_k^{\mathrm{H}})^2}{\Omega_k^2(t)}. \tag{4.16}$$

Hence $1/Z_k(t)$ is the renormalization which turns the approximated Hartree frequency into the exact effective frequency. In the previous section we have provided numerical evidence showing that $Z_k(t)$ takes a form quite close to the equilibrium one (at some time-dependent effective temperature) for $t \gtrsim t_0$ and, in particular, that it approaches unity rather fast as $k^2 > \overline{\phi^2}(t)$. As shown in Sec. IV E and in more detail in Appendix C, this holds for very late times of order $10^4 t_0$, close to complete lattice thermalization (necessarily cutoff dependent), with $Z_k(t)$ almost constant in time much earlier than $\overline{\phi^2}(t)$ or the power spectra and the effective temperature very close to the final equilibrium temperature. But it also holds for much shorter times, of order t_0 only, as soon as the universal cascade has set in, with $Z_k(t)$ almost constant as a

function of $k/[\overline{\phi^2}(t)]^{1/2}$ and some time-dependent effective temperature much larger than the final equilibrium temperature.

We tested the universality of this picture by studying the changes of Z_k (or absence thereof) upon changes of the lattice spacing, physical size, energy density, initial condensate, and microscopic details of initial conditions in our numerical evolutions.

Notice that we always use the exact classical time evolution for the fields and never the Hartree approximation to it. However, this exact evolution of the modes with $k^2 > \overline{\phi^2}(t)$ is well reproduced with an effective mass as given by the Hartree approximation Eq. (4.15).

In quantum theory, as is well known the definition of the number operator is not unique (see, for example, Refs. [6,7]). However, we can introduce a classical number of modes based in the correspondence principle. In the classical limit the number of quanta is given by the phase-space area encircled by the classical phase-space trajectory divided by 2π (in units where $\hbar = 1$). In the Hartree approximation both $\pi_{\boldsymbol{k}}(t)$ and $\phi_{\boldsymbol{k}}(t)$ oscillate with frequency $\Omega^{\mathrm{H}}_{\boldsymbol{k}}(t)$. The phase-space area for a slow varying frequency is then given by the ellipse area $\pi|\pi_{\boldsymbol{k}}|_{\max}|\phi_{\boldsymbol{k}}|_{\max}$ where in addition for harmonic oscillations $|\pi_{\boldsymbol{k}}|_{\max} = (2|\overline{\tilde{\pi}_{\boldsymbol{k}}}|^2)^{1/2}$ and $|\phi_{\boldsymbol{k}}|_{\max} = (2|\overline{\tilde{\phi}_{\boldsymbol{k}}}|^2)^{1/2}$. Therefore, the number of modes is given by

$$\overline{n}_{\boldsymbol{k}}(t) = [|\overline{\tilde{\pi}_{\boldsymbol{k}}}|^2(t)|\overline{\tilde{\phi}_{\boldsymbol{k}}}|^2(t)]^{1/2}. \tag{4.17}$$

Also,

$$\overline{n}_{\boldsymbol{k}}(t) = \frac{1}{2}\frac{\sqrt{Z_k(t)}}{\Omega^{\mathrm{H}}_{\boldsymbol{k}}(t)}\overline{|\tilde{\pi}_k|^2}(t) + \frac{1}{2}\frac{\Omega^{\mathrm{H}}_{\boldsymbol{k}}(t)}{\sqrt{Z_k(t)}}\overline{|\tilde{\phi}_k|^2}(t),$$

where we used the continuum limit of Eq. (4.16), namely,

$$Z_k(t)\overline{|\tilde{\pi}_k|^2}(t) = [\Omega^{\mathrm{H}}_{\boldsymbol{k}}(t)]^2\overline{|\tilde{\phi}_k|^2}(t). \tag{4.18}$$

Although derived within the assumption of harmonic oscillations with a slowly varying frequency, Eq. (4.17) should have a more general validity, since $n_{\boldsymbol{k}}$ provides in any case a measure of the phase space occupied by the trajectory of the $\boldsymbol{k}$ mode. The only important condition is that the different modes are weakly coupled. This is true, when the UV cascade has fully developed, for all $\boldsymbol{k}$ such that $[\overline{\phi^2}(t)]^{1/2} < |\boldsymbol{k}| \lesssim \overline{k}(t)$, where $[\overline{\phi^2}(t)]^{1/2}$ decreases with time tending to a small equilibrium value $\sqrt{\langle\phi^2\rangle}$ of order $\sqrt{T/a} \sim a\sqrt{E/V}$. Furthermore, if t is not too large so that $\overline{k}(t) \ll \Lambda$, then the occupied modes do not feel the lattice discretization and have the relativistic dispersion relation. Therefore

$$\overline{n}_{\boldsymbol{k}}(t) = \frac{\sqrt{Z_k(t)}}{\Omega^{\mathrm{H}}_{\boldsymbol{k}}(t)}\overline{|\tilde{\pi}_{\boldsymbol{k}}|^2}(t), \tag{4.19}$$

where now $[\Omega^{\mathrm{H}}_{\boldsymbol{k}}(t)]^2 = k^2 + 1 + 3\overline{\phi^2}(t)$.

We plot in Fig. 28 the number of modes over spherical shells, $4\pi k^2\overline{n}_k(t)$, vs $k = |\boldsymbol{k}|$ at different times. Figure 28 should be compared with Figs. 13 and 14 since $\overline{n}_k(t)$ and $\overline{|\tilde{\pi}_{\boldsymbol{k}}|^2}(t)$ are related through Eq. (4.19). One sees that the main dependence of $\overline{n}_k(t)$ on k comes from $\overline{|\tilde{\pi}_{\boldsymbol{k}}|^2}(t)$.

Notice that Eq. (4.19) can be written in terms of the effective frequency $\Omega_k(t)$ as

$$\overline{n}_{\boldsymbol{k}}(t) = \frac{\overline{|\tilde{\pi}_{\boldsymbol{k}}|^2}(t)}{\Omega_k(t)}$$

which is the classical equilibrium occupation number with the temperature replaced by $\overline{|\tilde{\pi}_{\boldsymbol{k}}|^2}(t)$. In fact, in thermal equilibrium the power spectrum and the temperature are related by Eq. (3.4). During the UV cascade we are in a situation of effective equilibration for times t later than $t_0 \sim 500$ as shown by Fig. 10 and the results of Sec. IV F. However, $\overline{|\tilde{\pi}_{\boldsymbol{k}}|^2}(t)$ depends both on time and on the wave number as depicted in Figs. 16, 18, and 25. In addition, the k modes with $k^2 < \overline{\phi^2}(t)$ only thermalize for times of the order 10^6 as we see in Fig. 25. This makes it awkward to try and interpret $\overline{|\tilde{\pi}_{\boldsymbol{k}}|^2}(t)$ as a k-dependent effective temperature since an equilibrium or quasiequilibrium state should depend only on a few macroscopic parameters (with one playing the role of temperature) varying slowly in time. Notice however that $\overline{|\tilde{\pi}_{\boldsymbol{k}}|^2}(t)$ decreases both with time and with the wave number k for $k^2 > \overline{\phi^2}(t)$ [see Figs. 16, 18, and 25] and does that in a very smooth and regular way. This suggests indeed the existence of a few slowly time-dependent parameters, not dependent on the details of the initial conditions, which govern the evolution of the cas-

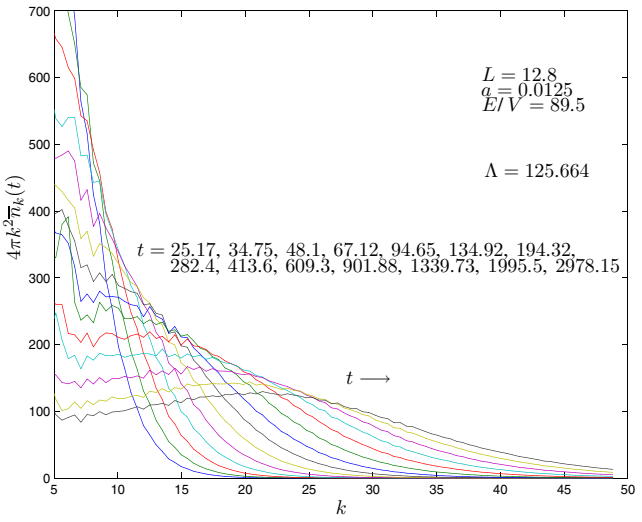

FIG. 28 (color online). The number of modes over spherical shells, $4\pi k^2\overline{n}_k(t)$, vs $k = |\boldsymbol{k}|$ at the different times indicated. The initial conditions are infrared random plane waves. The UV cascade is clearly seen as $k^2\overline{n}_k(t)$ is depleted for low k while it grows for large k as time grows.

cade for $k^2 > \overline{\phi^2}(t)$. Notice that instead $\overline{|\tilde{\pi}_{\boldsymbol{k}}|^2}(t)$ increases as well as decreases with k and t for the modes $k^2 < \overline{\phi^2}(t)$ in a much more erratic way strongly dependent on the detail of the initial conditions (see Figs. 16, 24, and 25).

H. Effective mass squared

The time averaging defined by Eq. (2.17) is intended to eliminate the microscopic oscillations of the field. We illustrate such microscopic behavior in Fig. 31 showing the field $\phi(\boldsymbol{x}, t)$ averaged over the space. The frequency of the time oscillation can be therefore considered as the effective mass $M_{\rm eff}(t)$ of the field. Moreover, by Fourier transforming the field $\phi(\boldsymbol{x}, t)$ we obtain frequencies $\Omega_{\boldsymbol{k}}$ numerically. This procedure is more costly than Eq. (4.13) but we find an excellent agreement between both. We want to stress that for this to happen it is necessary that the space-time discretization scheme in the numerics treats space and time on equal footing, as ours does (see Sec. II C). Notice also that the use of lattice expressions like Eq. (4.13), valid in principle to all orders in a, is very efficient and convenient to compare results on lattices with different lattice spacings.

It must be noticed that the fast oscillations displayed in Fig. 31 are erased by the time averaging. Thanks to such averaging the slow dynamics becomes visible through Figs. 4–25.

We plot in Fig. 29 $[M^2_{\rm eff}(t) - 1]$ vs the logarithm of time for different values of $\rho \equiv E/V$. Notice that $M^2_{\rm eff}(t)$ monotonically decreases with time while the UV cascade develops. We see that $M^2_{\rm eff}(t) > 1$ and that it decreases with ρ. Indeed, $M^2_{\rm eff}(t) \to 1$ (its linearized value) for $\rho \to 0$. We find that $M^2_{\rm eff}(t) - 1$ is approximately proportional to $\overline{\phi^2}(t)$.

We depict in Fig. 30 the ratio

$$R \equiv \frac{M^2_{\rm eff}(t) - 1}{\overline{\phi^2}(t)}, \tag{4.20}$$

as a function of $\log t$. We see that R is approximately time independent and that it decreases with E/V. It should be noticed that R always stays below the value $R_{\rm H} = 3$ predicted by the Hartree approximation [9] and well above the value $R_{\text{Large } N} = 1$ corresponding to the large number of components limit.

In summary, we find that $M^2_{\rm eff}(t)$ can be written as

$$M^2_{\rm eff}(t) = 1 + R(\rho)\overline{\phi^2}(t), \tag{4.21}$$

where $1.5 < R(\rho) < 3$ is approximately time independent and decreases with ρ.

We analyze the cnoidal solution in Appendix C and compute its effective mass. The parameter R for the cnoidal solution turns out to be between $\frac{3}{2}$ and $\frac{\pi}{2}$ and is depicted in Fig. 33.

As discussed in Sec. IV G the modes with $k^2 \gg \overline{\phi^2}(t)$ are governed by the Hartree mass $1 + 3\ \overline{\phi^2}(t)$ while the $k = 0$ mode oscillates according to $M_{\rm eff}(t)$. The Hartree mass and $M^2_{\rm eff}(t)$ are substantially different as remarked above.

Moreover, $M_{\rm eff}(t)$ governs the long-range behavior of the correlators as real space. The two-point correlator tends to zero for long distances as

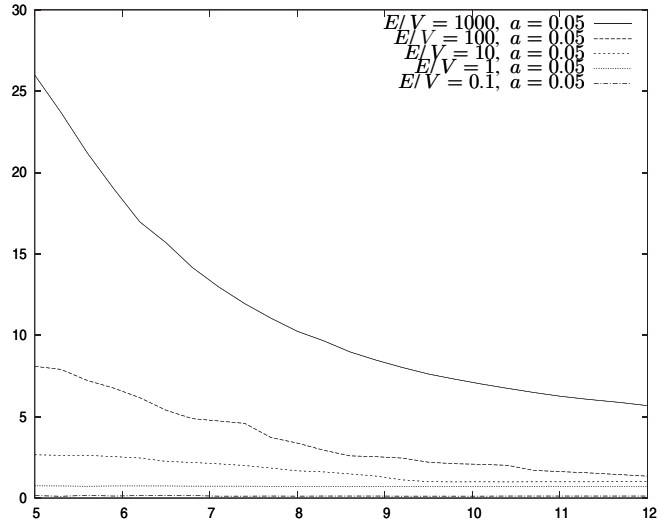

FIG. 29. $M^2_{\rm eff}(t) - 1$ as a function of the logarithm of the time t for $E/V = 0.1$, 10, 100, and 1000 with $L = 6.4$ and $a = 0.1$. No average is performed over initial packet amplitudes or positions. Time averaging is performed here as by Eqs. (2.17) and (2.18).

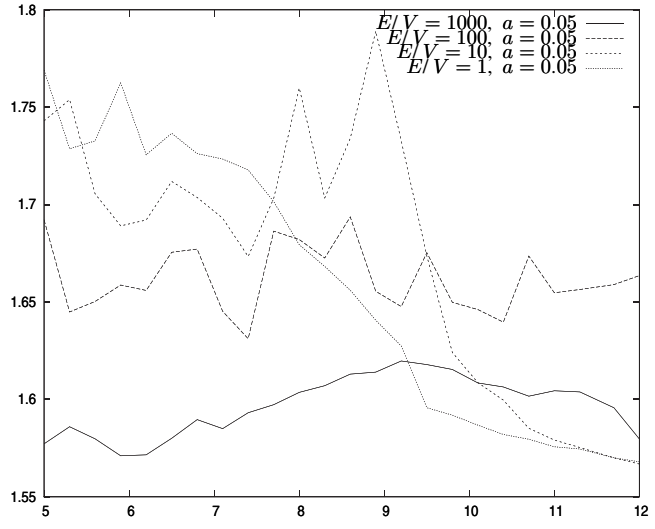

FIG. 30. $R \equiv [M^2_{\rm eff}(t) - 1]/\overline{\phi^2}(t)$ as a function of the logarithm of time t for $E/V = 0.1$, 10, 100, and $E/V = 1000$ with $L = 6.4$ and $a = 0.1$. Notice that R varies in a much narrower interval than $M^2_{\rm eff}(t)$ depicted in Fig. 29. No average is performed over initial packet amplitudes or positions. Time averaging is performed here as by Eqs. (2.17) and (2.18).

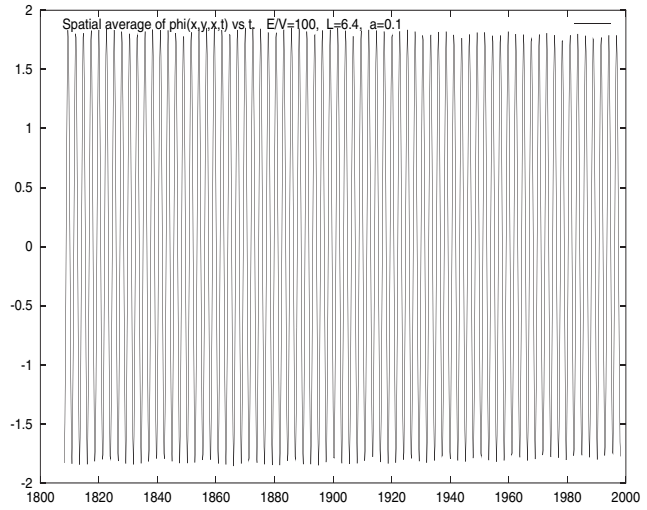

FIG. 31. The space average of $\phi(\boldsymbol{x}, t)$ as a function of time t for $E/V = 100$ with $L = 6.4$ and $a = 0.1$ over a sample time interval. Notice the fast oscillations displayed here which are erased by the time averaging. Thanks to time averaging the slow dynamics becomes visible in Figs. 4–25.

$$C(x) \overset{x\gg a}{=} C_0 \frac{e^{-M_{\rm eff}(t)x}}{x},$$

where C_0 is a constant.

In summary, modes with k^2 below and above $\overline{\phi^2}(t)$ are governed by different masses. The former by $M^2_{\rm eff}(t) \simeq 1 + 1.5\ \overline{\phi^2}(t)$ and the latter by the Hartree mass $1 + 3\ \overline{\phi^2}(t)$. Clearly, the long-range behavior of the correlators is governed by the low momentum mass $M_{\rm eff}(t)$.

I. The slow dynamics of the infrared modes and effective thermalization

The picture of the averaged dynamics for late times in the lattice model is as follows:

(i) The modes with $k^2 > \overline{\phi^2}(t)$ effectively thermalize with a time-dependent temperature while they obey the Hartree approximation. That is, their dynamics is weakly nonlinear.

(ii) The modes with $0 \le k^2 \lesssim \overline{\phi^2}(t)$ keep interacting quite strongly between them. They thermalize much later than the rest of the modes.

(iii) Both sets of modes keep interacting with each other.

There are definitely two time scales for thermalization. The shorter one $t_0 \sim 500$ describes the effective thermalization of the Hartree modes while the time scale for the effective thermalization of the infrared modes is much longer than t_0 and of the order $\sim 10^6$.

The modes with $0 \le k^2 \lesssim \overline{\phi^2}(t)$ manifest in the IR behavior of the correlator as a long-lived inhomogeneous condensate. This condensate keeps interacting with the higher k modes which behave as a thermal bath in contact with it. Notice that the mode distribution becomes time independent on the lattice for late times. Hence, the field correlator is a static function described by the Fourier transform of

$$|\tilde{\phi}_k|^2 = \frac{TZ_k}{k^2 + 1 + 3\overline{\phi^2}(t)}, \tag{4.22}$$

where T is the asymptotic time limit of $\overline{|\tilde{\pi}_k|^2}(t)$.

While $M^2_{\rm eff}$ decreases with a time scale $\sim t_0$ (see Fig. 29), Z_k varies with an even longer time scale $\sim 10^6$. It is akin to a k-dependent wave function renormalization which becomes the unit for $k^2 \gg \overline{\phi^2}(t)$.

It should be stressed that the inhomogeneous condensate is not a classical solution of the ϕ^4 equations (2.3). It is a classical statistical configuration that can be seen only through the correlators like $\overline{\phi\phi}(\boldsymbol{x}, t)$. Moreover, the average value of ϕ just vanishes for late times as shown in Fig. 9.

Notice that the local observables as $\overline{\pi^2}(t)$, $\overline{(\nabla\phi)^2}(t)$, $\overline{\phi^2}(t)$, and $\overline{\phi^4_+}(t)$ are dominated by the modes with $k^2 \gtrsim \overline{\phi^2}(t)$. This explains that the thermal equilibrium curve approximately agrees (to 90%) with time averages in Fig. 10 although the infrared modes are not yet completely thermalized.

Extensive numerical calculations varying the initial conditions showed us that the thermalization dynamics including the UV cascade possess a universal character. That is, the UV cascade exhibits the same features for different kinds of initial conditions (plane waves, localized packets, etc.) with initial power in the infrared modes ($k \lesssim 30\pi/L \ll \pi/[2a]$) and energy density not too small ($\rho \gtrsim 1$).

In the continuum theory the ultraviolet cascade continues forever and therefore, for finite energy densities, the system will reach thermal equilibrium for infinite times at zero temperature. The inhomogeneous condensate thus disappears for extremely long times in the continuum theory.

As the inhomogeneous condensate is an infrared phenomena, it should be present in quantum theory for large occupation numbers and weak coupling. In other words, the low k behavior of Z_k should not change in quantum theory when such conditions are fulfilled.

V. DISCUSSIONS AND CONCLUSIONS

The present work shows that a UV cascade enjoying universal properties is the basic mechanism of thermalization both in 3 + 1 and 1 + 1 dimensions [9]. Although we are not in a position to derive the properties of this cascade from the microscopic equation of motion (2.3), it is easy to see from Eq. (2.3) that energy should flow towards higher wave numbers. Assume we start from a plane wave initial condition

$$\phi(0,\boldsymbol{x}) = A\cos(\boldsymbol{k}\cdot\boldsymbol{x}), \qquad \dot{\phi}(0,\boldsymbol{x}) = A\sin(\boldsymbol{k}\cdot\boldsymbol{x}),$$

where A is a constant. The nonlinear term ϕ^3 in Eq. (2.3) will immediately generate higher harmonics: $\cos(3\boldsymbol{k}\cdot\boldsymbol{x})$, $\cos(9\boldsymbol{k}\cdot\boldsymbol{x})$, $\cos(5\boldsymbol{k}\cdot\boldsymbol{x})$, etc. That is, energy is moving to higher wave numbers.

Moreover, if we consider a superposition of plane waves as an initial condition,

$$\phi(0,\boldsymbol{x}) = \sum_{a=1}^{n} A_a\cos(\boldsymbol{k}_a\cdot\boldsymbol{x}),$$

$$\dot{\phi}(0,\boldsymbol{x}) = \sum_{a=1}^{n} A_a\sin(\boldsymbol{k}_a\cdot\boldsymbol{x}),$$

the interaction term ϕ^3 generates sums and differences: $\boldsymbol{k}_a \pm \boldsymbol{k}_b \pm \boldsymbol{k}_c$ etc., for $a, b, c = 1, \ldots, n$. This implies energy flowing both for increasing and for decreasing wave numbers.

Notice that this mode mixing takes place very fast, at the microscopic time scale, that is, a unit time scale in dimensionless variables. The UV cascade we observe happens in a much longer time scale. This means that these fast microscopic processes combine in a nontrivial way resulting on a UV cascade with a slow time scale.

It is important to estimate to which extent the present results can be applied in quantum theory. A necessary condition for the validity of the classical approximation is that the occupation numbers must be large. The relevant occupation numbers decrease during the UV cascade due to the modes flowing towards unoccupied high wave number slots. Hence, if the classical approximation is valid for late times, it will be valid earlier (as is the case in 1 + 1 dimensions [9]). A simple criterion for the validity of the classical approximation in QFT at thermal equilibrium is that

$$T_p \gg \omega_p(k_p), \tag{5.1}$$

where $\omega_p(k_p) = \sqrt{k_p^2 + M_{p,\mathrm{eff}}^2}$ are the dimension-full frequencies.

In dimensionless variables Eq. (5.1) takes the form,

$$\frac{T}{\lambda} \gg \sqrt{k^2 + M_{\mathrm{eff}}^2} > M_{\mathrm{eff}}. \tag{5.2}$$

Following Eq. (4.21) we obtain as an estimate for M_{eff}^2 from our numerical results

$$M_{\mathrm{eff}}^2 \sim 1 + A\sqrt{\rho}, \tag{5.3}$$

where $\rho = \frac{E}{V}$ and $A \sim 0.2$–0.5.

For $\rho \gtrsim 1$ we thus find that the classical approximation applies for

$$\lambda \ll (2a)^3\rho^{3/4}, \tag{5.4}$$

where we used that $T = (2a)^3\rho$ for small a [Eq. (3.9)].

For $\rho \lesssim 1$ we instead find that the classical approximation applies for

$$\lambda \ll (2a)^3\rho. \tag{5.5}$$

Both Eqs. (5.4) and (5.5) lead to small values of the coupling λ since the spacing a must be itself small to avoid lattice effects. However, in inflationary theories very small values of $\lambda \sim 10^{-12}$ are customary (in order to agree with the smallness of the CMB anisotropy) which leaves room for the use of the classical approximation.

As stated above the validity of the classical approximation decreases with time. Let us estimate the time where it ceases to be valid.

The total energy density can be estimated in terms of the average occupation number $\overline{n_k}$ (where the average is here over the $\vec{k}$ modes) as follows:

$$\rho \sim \overline{k}^3\overline{n_k}\sqrt{\overline{k}^2 + M_{\mathrm{eff}}^2}.$$

The classical approximation holds if the occupation numbers are large for the relevant modes. Therefore, a necessary condition is

$$\frac{\overline{n_k}}{\lambda} \gg 1,$$

since the coupling λ has been absorbed in the field redefinition Eq. (2.2).

In the ultrarelativistic regime $\overline{k} \gg M_{\mathrm{eff}}$ we have

$$\overline{k}^4 \ll \frac{\rho}{\lambda} \quad \text{and therefore} \quad \overline{k} \ll \left(\frac{\rho}{\lambda}\right)^{1/4}, \tag{5.6}$$

while in the nonrelativistic domain $\overline{k} \ll M_{\mathrm{eff}}$ we have

$$M_{\mathrm{eff}}\overline{k}^3 \ll \frac{\rho}{\lambda}$$

and hence using Eq. (5.3)

$$\overline{k}^3 \ll \frac{\rho^{3/4}}{\lambda} \quad \text{and therefore} \quad \overline{k} \ll \frac{\rho^{1/4}}{\lambda^{1/3}}. \tag{5.7}$$

Since $\lambda \ll 1$,

$$\frac{1}{\lambda^{1/3}} \gg \frac{1}{\lambda^{1/4}}, \qquad \text{thus } \left(\frac{\rho}{\lambda}\right)^{1/4} \ll \frac{\rho^{1/4}}{\lambda^{1/3}},$$

and the ultrarelativistic condition Eq. (5.6) is more stringent than the nonrelativistic bound Eq. (5.7). We can therefore always use the condition Eq. (5.6) for the validity of the classical approximation.

Using now Eq. (4.7) for $\overline{k}(t)$ yields in both regimes that the classical approximation is valid for times t

$$t \ll t_{\max} \simeq \frac{\rho^{3/4}}{\lambda^{3/4}k_0^3}. \tag{5.8}$$

The conditions Eqs. (5.5) and (5.6) are compatible since $\overline{k} < \pi/2a$. Therefore, Eq. (5.6) implies

$$\frac{\pi}{2a} \ll \left(\frac{\rho}{\lambda}\right)^{1/4} \quad \text{and then}$$

$$(2a)^3\rho^{3/4} \gg \pi^3\lambda^{3/4} \text{or} \frac{\rho}{\lambda} \gg \left(\frac{\pi}{2a}\right)^4,$$

which is more stringent than Eq. (5.4).

In summary, the classical approximation is valid for times earlier than $t_{\max}$ [given by Eq. (5.8)] provided

$$\frac{\rho}{\lambda} \gg \left(\frac{\pi}{2a}\right)^4, \tag{5.9}$$

that is, high density (large occupation numbers) and/or small coupling. This condition constrains the initial conditions which fix ρ. Notice that the coupling λ does have an intrinsic meaning in the quantum theory.

A condition for the validity of the classical dynamics in QFT is derived for high density in Ref. [11] in the context of the $2PI$-$1/N$ approach. For further studies about the validity of the classical approximation in different contexts see [18,20,26].

Let us now comment on the character of the universal stage. The dimensionality of the space plays a crucial role in this phenomenon. In one space dimension effective thermalization takes place much faster in analogous conditions [9]. Here, in $3 + 1$ dimensions a second and even longer time scale appears characterizing the thermalization of infrared modes with $k < \sqrt{\overline{\phi^2}}(t)$. The infrared modes keep interacting for far longer times than the higher k modes. In $3 + 1$ dimensions the infrared modes thermalize the last while in $1 + 1$ dimensions they thermalize the first [9].

The UV cascade is clearly less efficient in three space dimensions to fill the higher k modes pumping energy from the low k modes. Clearly, in one space dimension the phase space is dramatically small making the UV cascade very efficient.

The same phase-space effect (k^2) in three space dimensions makes the classical statistical mechanics of the ϕ^4 theory divergent due to the ultraviolet catastrophe.

All this suggests that thermalization is reached in quantum theory too as recent works (including memory effects) indicate [10–12]. Moreover, for large initial occupation numbers and small coupling the classical regime should correctly describe the evolution of the theory till a time $t_{\max}$ [see Eq. (5.8)].

A remarkable feature of the thermalization mechanism is that even starting from a completely classical regime (large occupation numbers at low wave numbers), the UV cascade depletes these modes and fills the high ones. Therefore, at some time $\sim t_{\max}$ (that could be very long) quantum physics unavoidably shows up. This is the out-of-equilibrium counterpart to the fact that classical statistical mechanics is ill defined due to the ultraviolet catastrophe which can be cured only by the quantum treatment.

Thermalization implies to forget everything about the initial conditions except (obviously) the conserved quantities like energy, momentum, and angular momentum. The thermalization is therefore expected to substantially change for integrable theories where the number of conserved quantities equals the number of degrees of freedom.

In this paper we solve the exact microscopic dynamics and then we averaged on time intervals and space in order to derive the slow dynamics we are interested in. This is perfectly correct but a lot of information is first obtained and then dumped in the averaging process. Alternatively a transport approach could be followed deriving equations for the observables in macroscopic time scales and then solve them. We mean to derive transport equations of the Boltzmann or Fokker-Planck type.

ACKNOWLEDGMENTS

Its a pleasure to thank D. Boyanovsky for useful discussions. The numerical calculations were performed on clusters of personal computers at LPTHE-Paris and at the Physics Department of Milano-Bicocca; the simulations with largest lattices were performed on the Avogadro cluster of CILEA.

APPENDIX A: AVERAGE OVER DISCRETE DIRECTIONS

The space discretization and the finite size spoil the rotational invariance of the continuum infinite-volume Hamiltonian. This implies the same invariance for the classical field equation and for the equilibrium averages (see Sec. III). Rotational invariance should be recovered at short distances when $a \to 0$ and at long distances when $L \to \infty$. Thus any lattice observable on the wave numbers cube $(2\pi/L)C_N$ that corresponds to a rotational invariant observable of the continuum infinite-volume theory should depend only on k^2 when $a \to 0$ and $kL \gg 1$ or when $L \to \infty$ and $ka \ll 1$ (a similar argument would apply for the x-space cube $2aC_N$). To verify the onset of rotational invariance in nonperturbative or numerical lattice calculations is usually quite costly and often not even necessary. In fact, by turning the argument around and assuming that rotational invariance will be recovered in the appropriate limits, one can greatly reduce fluctuations by performing an average over all directions on discrete observables. This can be done as follows.

Given any array $f_{\boldsymbol{n}}$ over C_N, we consider its average over discrete directions $\bar{f}_n$ as

$$\bar{f}_n = \frac{1}{S_n} \sum_{\boldsymbol{n} \in C_N} \theta(n \le |\boldsymbol{n}| < n + 1) f_{\boldsymbol{n}}, \qquad n = 0, 1, 2, \ldots, \sqrt{3}N/2, \tag{A1}$$

where $\theta(\cdots) = 1$ (0) if its arguments is true (false) and S_n is the number of points of C_N at a distance d from the

origin such that $n \le d < n+1$; that is

$$S_n = \sum_{\boldsymbol{n}\in C_N} \theta(n \le |\boldsymbol{n}| < n+1).$$

Up to purely geometrical fluctuations, S_n grows like $4\pi n^2$ for n up to $N/2$, while for $N/2 < n \le \sqrt{3}N/2$, in the corners of the cube, its shrinks to zero. To fix a specific value of the radius of this spherical shell, we choose the average distance of all lattice points within the shell

$$r_n = \frac{1}{S_n}\sum_{\boldsymbol{n}\in C_N} \theta(n \le |\boldsymbol{n}| < n+1)|\boldsymbol{n}|.$$

When plotted against r_n, S_n still has purely geometrical fluctuations with respect to the continuum expression, most noticeably at $n = 0$, where $S_0 = 1$ while $4\pi r_0^2 = 0$. Of course, averaging over several consecutive shells would reduce these geometric fluctuations. Such an average is in fact automatic in the limit $L \to \infty$ of continuous wave numbers, since in any physical realizable measure there exists a finite resolution Δk independent of L. On the other hand the limit $L \to \infty$ is not feasible in numerical calculations and one has to find the correct balance between size and control of fluctuations.

Suppose now that the array $f_{\boldsymbol{n}}$ is the finite size version of the continuous function $f(\boldsymbol{k})$ over the first Brillouin zone at infinite size [the argument would apply also if $f_{\boldsymbol{n}}$ were the lattice version of a continuous $f(\boldsymbol{x})$ on the cubic volume V]. Then $\bar{f}_n$ provides a finite size version of the angle average of $\bar{f}(k)$ of $f(\boldsymbol{k})$, where $k = |\boldsymbol{k}|$. In other words, the discrete plot of $\bar{f}_n$ vs $k_n \equiv (2\pi/L)r_n$ provides an approximation of the continuous plot of $\bar{f}(k)$ vs k, if $L \to \infty$ at fixed a and $f_{\boldsymbol{n}}$ has indeed a continuous limit. If this limit is rotational invariant all physical information is stored in f as a function of k only; thus the average over all solid angles in the continuum has no effect at all, $\bar{f} = f$, while the average over discrete shells S_n greatly reduces the statistical fluctuations.

APPENDIX B: LINEARIZED DISCRETE DYNAMICS

It is instructive to study first the discrete field equation (2.12) at the linearized level. Thus we consider the case of a uniform field $\phi(\boldsymbol{x}, t) = \phi(t)$, namely, the recursion

$$\phi(t+a) + \phi(t-a) = \frac{2\phi(t)}{1 + \frac{1}{2}a^2[1+\phi^2(t)]}. \tag{B1}$$

Given $\phi(0)$ and $\phi(a)$, this recursion determines $\phi(t)$ for the discrete times $t = na$, $n = 2, 3, \ldots$, yielding the discrete version of the well-known cnoidal uniform solution of the continuum equation (2.3).

We now linearize the generic $\phi(\boldsymbol{x}, t)$ around $\phi(t)$ by setting $\phi(\boldsymbol{x}, t) = \phi(t) + \eta(\boldsymbol{x}, t)$, where $\eta(\boldsymbol{x}, t)$ has vanishing space integral; this yields the linear recursion

$$\eta(\boldsymbol{x}, t+a) + \eta(\boldsymbol{x}, t-a) = \frac{1}{4}B(\phi)\sum_{\boldsymbol{\sigma}} \eta(\boldsymbol{x} + a\boldsymbol{\sigma}, t), \tag{B2}$$

where $B(\phi)$ is given by Eq. (3.26). In terms of Fourier modes we have

$$\eta(\boldsymbol{x}, t) = V^{-1/2}\sum_{\boldsymbol{k}\neq\boldsymbol{0}} \tilde{\phi}_{\boldsymbol{k}}(t) e^{i\boldsymbol{k}\cdot\boldsymbol{x}}$$

and Eq. (B2) entails, for $\boldsymbol{k} \neq \boldsymbol{0}$,

$$\tilde{\phi}_{\boldsymbol{k}}(t+a) + \tilde{\phi}_{\boldsymbol{k}}(t-a) = 2\tilde{\phi}_{\boldsymbol{k}}(t)\cos\omega_{\boldsymbol{k}}(t), \tag{B3}$$

where the instantaneous frequency $\omega_{\boldsymbol{k}}(t)$ is fixed by the dispersion rule

$$\cos[\omega_{\boldsymbol{k}}(t)a] = B[\phi(t)]\prod_{j=1}^{D}\cos k_j a \tag{B4}$$

as a function of the wave number vector $\boldsymbol{k} \neq \boldsymbol{0}$. Equation (B3) is our lattice version of the Lamé equation governing the linearization of the continuum field equation over the cnoidal. In fact, in the continuum limit $a \to 0$, for any fixed $\boldsymbol{k}$ we have

$$\cos[\omega_{\boldsymbol{k}}(t)a] = 1 - \tfrac{1}{2}a^2[k^2 + 1 + 3\phi^2(t)] + \mathcal{O}(a^4)$$

so that Eq. (B2) becomes indeed

$$\left[\frac{d^2}{dt^2} + k^2 + 1 + 3\phi^2(t)\right]\tilde{\phi}_{\boldsymbol{k}}(t) = 0 \tag{B5}$$

with $\phi(t)$ solving now $\ddot{\phi} + \phi + \phi^3 = 0$ that is the cnoidal solution.

In the trivial case $\phi = 0$, which corresponds to the free-field case, the general solution of Eq. (B3) is straightforward and can be written

$$\tilde{\phi}_{\boldsymbol{k}}(t) = A_{\boldsymbol{k}} e^{-i\omega_{\boldsymbol{k}}t} + A^*_{-\boldsymbol{k}} e^{i\omega_{\boldsymbol{k}}t}$$

in terms of the constant amplitudes $A_{\boldsymbol{k}}$ fixed by the initial conditions. In this case $\omega_{\boldsymbol{k}}$ solves Eq. (B4) with $B(0) = (1 + a^2/2)^{-1}$ and is constant in time. Then recalling the general relation Eq. (3.22) we obtain

$$\tilde{\pi}_{\boldsymbol{k}}(t) \simeq -i\frac{\sin(\omega_{\boldsymbol{k}}a)}{a}(A_{\boldsymbol{k}} e^{-i\omega_{\boldsymbol{k}}t} - A^*_{-\boldsymbol{k}} e^{i\omega_{\boldsymbol{k}}t}) \mp \frac{a^2}{2}\tilde{\phi}_{\boldsymbol{k}}(t) \times \cos(\omega_{\boldsymbol{k}}a).$$

Finally, since time averages over several mode oscillations kill the interference between the positive frequency and the negative frequency terms in the power spectra, we find in this $\phi = 0$ case the following lattice version of the well-known virial theorem for harmonic oscillations

$$\overline{|\tilde{\pi}_{\boldsymbol{k}}|^2} = \frac{1}{a^2}\left[1 - \left(1 - \frac{1}{4}a^4\right)\cos^2(\omega_{\boldsymbol{k}} a)\right]\overline{|\tilde{\phi}_{\boldsymbol{k}}|^2}$$
$$= \frac{1}{a^2}\left[1 - \frac{1 - \frac{1}{2}a^2}{1 + \frac{1}{2}a^2}\prod_{j=1}^{D}\cos^2 k_j a\right]\overline{|\tilde{\phi}_{\boldsymbol{k}}|^2}, \qquad \text{(B6)}$$

where the dispersion relation Eq. (B4) was used with $\phi = 0$. In the limit $a \to 0$ Eq. (B6) reduces to

$$\overline{|\tilde{\pi}_k|^2}(t) = (k^2 + 1)\overline{|\tilde{\phi}_k|^2}(t)$$

as expected.

When $\phi \neq 0$ we may still write the general solution of the recursion (B2) as

$$\tilde{\phi}_{\,k}(t) = A_{\boldsymbol{k}} z_{\boldsymbol{k}}(t) + A^*_{-\boldsymbol{k}} z^*_{\boldsymbol{k}}(t),$$

where the amplitudes $A_{\boldsymbol{k}}$ are constant in time while $z_{\boldsymbol{k}}(t) = z_{-\boldsymbol{k}}(t)$ solves Eq. (B2) with initial conditions

$$z_{\boldsymbol{k}}(0) = 1, \qquad z_{\boldsymbol{k}}(a) = e^{-i\omega_{\boldsymbol{k}}(0)a}.$$

Equation (B5) admits close form solutions when ϕ is given by the cnoidal solution Eq. (D1). In particular, the forbidden band for $k^2 > 0$ corresponds to

$$\tfrac{1}{2}\phi_0^2 + 3 \le k^2 \le \sqrt{\tfrac{1}{3}\phi_0^4 + 2\phi_0^2 + 4} + 1 \qquad \text{(B7)}$$

(see, for example, [30]).

APPENDIX C: THE HARTREE APPROXIMATION FROM THE LATE TIME EXACT BEHAVIOR

We learn how to obtain the Hartree frequency on the lattice: we consider the discrete dynamics linearized as in Appendix B and replace the background $\phi_0^2(t)$ with $\overline{\phi^2}(t)$ in the dispersion relation Eq. (B4), obtaining

$$\cos(a\Omega_{\boldsymbol{k}}^{\xi \mathrm{H}}) = B[\xi\overline{\phi^2}(t)]\prod_{j=1}^{3}\cos k_j a, \qquad \text{(C1)}$$

where $B(\phi)$ is given by Eq. (3.26) and where for future use we introduced the parameter ξ to control the coupling with the background: if $\xi = 1$ we have the Hartree frequency; if $\xi = 0$ we have the free massive frequency Eq. (4.9). Intermediate values $0 < \xi < 1$ will actually be ruled out below by fitting the numerical data.

$\Omega_{\boldsymbol{k}}^{\xi \mathrm{H}}$ is a function of time through the background $\overline{\phi^2}(t)$. On the lattice $\overline{\phi^2}(t)$ will tend to a nonzero limit as $t \to \infty$. According to the Hartree dominance of the equilibrium $\langle|\tilde{\phi}_{\boldsymbol{k}}|^2\rangle$, from Eq. (4.14) we then see that $\Omega_{\boldsymbol{k}} \simeq \Omega_{\boldsymbol{k}}^{\mathrm{H}}$, provided the full effective frequency $\Omega_{\boldsymbol{k}}$ tends to $\Omega_{\boldsymbol{k}}^{\mathrm{eq}}$ as $t \to \infty$. It is therefore very important to compare $\Omega_{\boldsymbol{k}}^{\xi \mathrm{H}}$ with the full effective frequency $\Omega_{\boldsymbol{k}}$. Recall that the Hartree approximation is a good approximation if the modes are weakly interacting, since it neglects direct wave scatterings and allows energy transfer only through the uniform self-consistent background $\overline{\phi^2}(t)$.

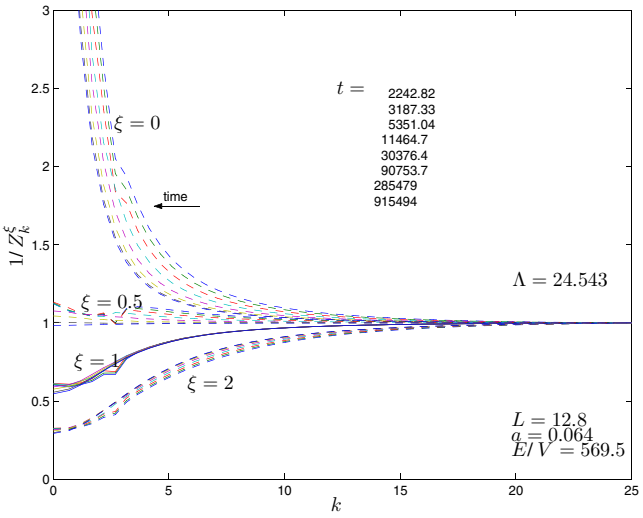

FIG. 32 (color online). The inverse of the ratio Z_k^{ξ} [defined by Eq. (C2)] vs the radial wave number for the values of time and of ξ indicated. All parameters are as in Fig. 22.

To perform the comparison we numerically average over discrete directions and study the ratio

$$Z_k^{(\xi)} \equiv \frac{\overline{|\tilde{\phi}_k|^2}}{a^2\overline{|\tilde{\pi}_k|^2}}\left[1 - \left(1 - \frac{1}{4}a^4\right)\cos^2(a\Omega_k^{\xi \mathrm{H}})\right]. \qquad \text{(C2)}$$

In Fig. 32 we plot $Z_k^{(0)}$, $Z_k^{(0.5)}$, $Z_k^{(1)}$, and $Z_k^{(1.5)}$ for several late times in the long evolution when π thermalized (see previous section). The Hartree value $\xi = 1$ clearly stands out as the most accurate in the time dependence: the curves at all different times almost perfectly collapse in a single curve, except that for very small wave numbers. All curves collapse for large k, regardless of the value of ξ, simply because when $k^2 \gg \overline{\phi^2}(t)$ any effect on the dispersion relation due to the background is negligible.

APPENDIX D: THE CNOIDAL SOLUTION

We discuss here the cnoidal solution of the ϕ^4 Eq. (2.3) that is the space-independent solution of $\ddot{\phi} + \phi + \phi^3 = 0$ explicitly given by

$$\phi(t) = \phi_0\,\mathrm{cn}(t\sqrt{1 + \phi_0^2}, k) \quad \text{with } k \equiv \frac{\phi_0}{\sqrt{2(1 + \phi_0^2)}}, \qquad \text{(D1)}$$

where $\mathrm{cn}(x, k)$ stands for the Jacobi cosinus of *module* k. This is a (doubly) periodic function satisfying $\phi(t) = -\phi(t + P)$, where $P = 2K(k)/\sqrt{1 + \phi_0^2}$ is the half-period and $K(k)$ stands for the complete elliptic integral.

The effective mass associated with this solution is therefore the basic frequency

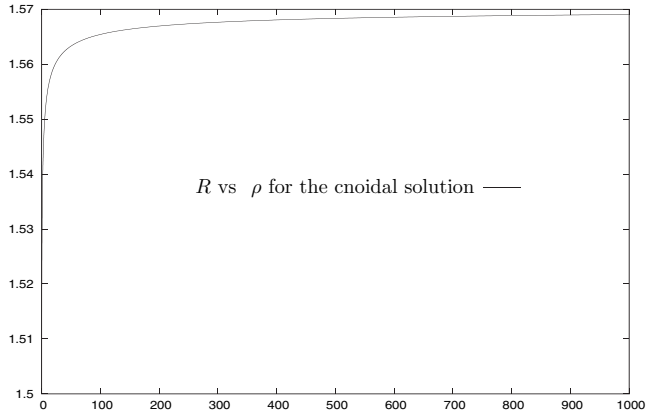

FIG. 33. $R(\phi_0) = [M_{\rm eff}^2 - 1]/ < \phi^2 >$ vs ρ for the cnoidal solution Eq. (D1). Here $\langle \cdots \rangle$ stands for the time average over one period.

$$M_{\rm eff} = \frac{2\pi}{2P} = \frac{\pi\sqrt{1+\phi_0^2}}{2K(k)}. \tag{D2}$$

The average value of the squared field over a period can be computed with the result [see Eq. (3.40) in Ref. [8]]

$$\langle \phi^2 \rangle = \frac{1}{2P}\int_0^{2P} dt \phi^2(t) = (1+\phi_0^2)\left[\frac{2E(k)}{K(k)} - 1\right] - 1. \tag{D3}$$

We plot in Fig. 33 the ratio $R(\phi_0) = (M_{\rm eff}^2 - 1)/\langle \phi^2 \rangle$ using Eqs. (D2) and (D3) [compare with Eq. (4.20)]. We plot it as a function of the energy density $\rho = \frac{1}{2}\phi_0^2(1 + \frac{1}{2}\phi_0^2)$.

We can compute analytically the function $R(\phi_0)$ for small and large arguments with the result

$$R(\phi_0) \overset{\phi_0 \to 0}{=} \frac{3}{2} + \mathcal{O}(\phi_0^2), \qquad R(\phi_0) \overset{\phi_0 \to \infty}{=} \frac{\pi}{2}.$$

In summary, $R(\phi_0)$ grows slowly and monotonically from the value $\frac{3}{2}$ to the value $\frac{\pi}{2}$ when ϕ_0 varies from zero to infinity.

The average value of $\dot{\phi}^2$ can be computed analogously with the result [see Eq. (3.60) in Ref. [8]]

$$\langle \dot{\phi}^2 \rangle = \frac{1}{3}(1+\phi_0^2)\left[\phi_0^2 + 2 - \frac{2E(k)}{K(k)}\right]. \tag{D4}$$

We find from Eqs. (D3) and (D4) using energy conservation,

$$\langle \phi^4 \rangle = \frac{1}{3}(\phi_0^4 + 6\phi_0^2 + 8) - \frac{8E(k)}{3K(k)}(1+\phi_0^2). \tag{D5}$$

Inserting Eqs. (D3)–(D5), for this homogeneous solution in the virial theorem Eq. (3.6) shows that this theorem is identically satisfied.

[1] E. Fermi, J. Pasta, and S. Ulam, *Note e Memorie* (Accademia dei Lincei, Roma, 1965), Vol. II (collected papers), p. 978.

[2] R. Livi, M. Pettini, S. Ruffo, M. Sparpaglione, and A. Vulpiani, Phys. Rev. A **28**, 3544 (1983); **31**, 1039 (1985); M. Pettini and M. Landolfi, Phys. Rev. A **41**, 768 (1990); J. DeLuca, A. J. Lichtenberg, and S. Ruffo, Phys. Rev. E **51**, 2877 (1995); **54**, 2329 (1996); **60**, 3781 (1999); J. DeLuca, A. J. Lichtenberg, and M. A. Lieberman, Chaos **5**, 283 (1995); G. Parisi, Europhys. Lett. **40**, 357 (1997).

[3] E. W. Kolb and M. S. Turner, *The Early Universe* (Addison-Wesley Publishing Company, Reading, MA, 1990).

[4] A. R. Liddle and D. H. Lyth, *Cosmological Inflation and Large Scale Structure* (Cambridge University Press, Cambridge, UK, 2000).

[5] D. Boyanovsky and H. J. de Vega, in *Proceedings of the VIIth Chalonge School on Current Topics in Astrofundamental Physics, Erice, Italy, 1999*, edited by N. G. Sanchez (Kluwer Academic, Dordrecht, 2001), Series C, Vol. 562, pp. 37–57.

[6] D. Boyanovsky, H. J. de Vega, R. Holman, D. S. Lee, and A. Singh, Phys. Rev. D **51**, 4419 (1995); D. Boyanovsky, D. Cormier, H. J. de Vega, and R. Holman, Phys. Rev. D **55**, 3373 (1997); D. Boyanovsky, D. Cormier, H. J. de Vega, R. Holman, A. Singh, and M. Srednicki, Phys. Rev. D **56**, 1939 (1997); D. Boyanovsky, D. Cormier, H. J. de Vega, R. Holman, and S. P. Kumar, Phys. Rev. D **57**, 2166 (1998).

[7] D. Boyanovsky, C. Destri, H. J. de Vega, R. Holman, and J. F. J. Salgado, Phys. Rev. D **57**, 7388 (1998).

[8] D. Boyanovsky, H. J. de Vega, R. Holman, and J. F. J. Salgado, Phys. Rev. D **54**, 7570 (1996).

[9] D. Boyanovsky, C. Destri, and H. J. de Vega, Phys. Rev. D **69**, 045003 (2004).

[10] J. Berges, Sz. Borsanyi, and J. Serreau, Nucl. Phys. **B660**, 51 (2003).

[11] J. Berges, hep-ph/0409233.

[12] S. Juchem, W. Cassing, and C. Greiner, Phys. Rev. D **69**, 025006 (2004).

[13] M. Gleiser and R. C. Howell, Phys. Rev. E **68**, 065203(R) (2003).

[14] G. Aarts, G. F. Bonini, and C. Wetterich, Phys. Rev. D **63**, 025012 (2001); Nucl. Phys. **B587**, 403 (2000).

[15] Sz. Borsanyi, A. Patkos, and D. Sexty, Phys. Rev. D **66**, 025014 (2002); **68**, 063512 (2003).

[16] J. Baacke and A. Heinen, Phys. Rev. D **69**, 083523 (2004).

[17] A. Arrizabalaga, J. Smit, and A. Tranberg, J. High Energy Phys. 10 (2004) 017.

[18] M. Salle, J. Smit, and J. C. Vink, Phys. Rev. D **64**, 025016

(2001); M. Salle and J. Smit, Phys. Rev. D **67**, 116006 (2003).

[19] J. I. Skullerud, J. Smit, and A. Tranberg, J. High Energy Phys. 08 (2003) 045.

[20] J. Smit and A. Tranberg, J. High Energy Phys. 12 (2002) 020; A. Tranberg and J. Smit, J. High Energy Phys. 11 (2003) 016; J. García-Bellido, M. García Pérez, and A. González-Arroyo, Phys. Rev. D **67**, 103501 (2003); **69**, 023504 (2004); G. D. Moore, J. High Energy Phys. 11 (2001) 021.

[21] R. Micha and I. I. Tkachev, Phys. Rev. Lett. **90**, 121301 (2003); Phys. Rev. D **70**, 043538 (2004).

[22] V. Zakharov, V. Lvov, and G. Falkovich, *Kolmogorov Spectra of Turbulence, Wave Turbulence* (Springer-Verlag, New York, 1992).

[23] See, for example, C. Destri, and H. J. de Vega, Nucl. Phys. **B290**, 363 (1987), and references therein.

[24] F. Zanlungo, thesis for the Italian ''Laurea in Fisica,'' Università Milano-Bicocca, 2002 (unpublished).

[25] See, for example, A. Milchev, D. W. Heermann, and K. Binder, J. Stat. Phys. **44**, 749 (1986); K. Binder and D. W. Heermann, *Monte Carlo Simulations in Statistical Physics*, Springer Series in Solid State Vol. 80 (Springer-Verlag, Berlin, 1988).

[26] J. Berges, Sz. Borsanyi, and C. Wetterich, Phys. Rev. Lett. **93**, 142002 (2004).

[27] J. Berges and J. Serreau, Phys. Rev. Lett. **91**, 111601 (2003).

[28] D. Boyanovsky, H. J. de Vega, R. Holman, and J. F. J. Salgado, Phys. Rev. D **59**, 125009 (1999).

[29] G. B. Whitham, *Linear and Nonlinear Waves* (John Wiley, New York, 1974).

[30] D. Boyanovsky, H. J. de Vega, and R. Holman, in *Proceedings of the Vth Chalonge School on Current Topics in Astrofundamental Physics, Erice, Italy, 1996* (World Scientific, Singapore, 1997), pp. 183–270.